Generation of plate tectonics with two-phase grain-damage and pinning: Source-sink model and toroidal flow

David Bercovici[a,*], Yanick Ricard[b]

[a] *Yale University, Department of Geology & Geophysics, New Haven CT, USA*
[b] *Laboratoire des Sciences de la Terre, CNRS, ENS, Université de Lyon, Lyon, France*

Abstract

The grain-damage and pinning mechanism of Bercovici and Ricard (2012) for lithospheric shear–localization is employed in two-dimensional flow calculations to test its ability to generate toroidal (strike-slip) motion and influence plate evolution. This mechanism posits that damage to the interface between phases in a polycrystalline material like peridotite (composed primarily of olivine and pyroxene) increases the number of small Zener pinning surfaces, which then constrain mineral grains to ever smaller sizes, regardless of creep mechanism. This effect allows a self-softening feedback in which damage and grain-reduction can co-exist with a grain-size dependent diffusion creep rheology; moreoever, grain growth and weak-zone healing are greatly impeded by Zener pinning thereby leading to long-lived relic weak zones. The fluid dynamical calculations employ source-sink driven flow as a proxy for convective poloidal flow (upwelling/downwelling and divergent/convergent motion), and the coupling of this flow with non-linear rheological mechanisms excites toroidal or strike-slip motion. The numerical experiments show that pure dislocation-creep rheology, and grain-damage without Zener pinning (as occurs in a single-phase assemblages) permit only weak localization and toroidal flow; however, the full grain-damage with pinning readily allows focussed localization and intense, plate-like toroidal motion and strike-slip deformation. Rapid plate motion changes are also tested with abrupt rotations of the source-sink field after a plate-like configuration is developed; the post-rotation flow and material property fields retain memory of the original configuration for extensive periods, leading to suboptimally aligned plate boundaries (e.g., strike-slip margins non-parallel to plate motion), oblique subduction, and highly localized, weak and long lived acute plate-boundary junctions such as at what is observed at the Aleutian-Kurile intersection. The grain-damage and pinning theory therefore readily satisfies key plate-tectonic metrics of localized toroidal motion and plate-boundary inheritance, and thus provides a predictive theory for the generation of plate tectonics on Earth and other planets.

Keywords: **Keywords:** Plate generation; mantle convection; damage mechanics

1. Introduction

Plate tectonics is arguably one of the most successful scientific theories in physical science, given its predictive capacity regarding, for example, the distribution and magnitude of seismic and volcanic disasters (see Abbott, 2011), or sea-floor ages and hydrocarbon maturation (see McKenzie, 1981). However it also plays a crucial role in planetary science since plate motion is a likely key ingredient for planetary habitability. In particular the plate-tectonic mode of mantle circulation drives chemical disequilibrium in the ocean and atmosphere by constantly bringing new mantle material to the surface. In this way, plate tectonics drives the geological carbon cycle through erosion, weathering and volcanism (Walker et al., 1981), which imposes a negative feedback and the long-term climate stability necessary for biological evolution over billions of years. Likewise, plate tectonics may also be necessary for the origin of life by providing an energy source for chemosynthetic life at the bottom of the ocean, i.e., at mid-ocean ridges (e.g., Southam and Westall, 2007). The discovery of many terrestrial planets in other solar systems over the last fifteen years (e.g., Charbonneau et al., 2009) has, therefore, emphasized the importance of understanding the conditions for plate tectonics as a possible requisite for biological habitability (Valencia, O'Connell, and Sasselov, 2007; Valencia and O'Connell, 2009; O'Neill and Lenardic, 2007; Landuyt and Bercovici, 2009b; Korenaga, 2010; van Heck and Tackley, 2011; Foley, Bercovici, and Landuyt, 2012).

However, understanding the conditions for plate tectonics requires a predictive theory for how it arises during the evolution of a planet, and in particular how it is generated by mantle convection on some but not all planets. For example, the occurrence of plate tectonics on Earth but not its putative twin Venus (or any of the other terrestrial planets in our solar system) is one of

*Corresponding author
Email addresses: david.bercovici@yale.edu (David Bercovici), yanick.ricard@ens-lyon.fr (Yanick Ricard)

the major enigmas in Earth and planetary science. While plate tectonics is well recognized to be a manifestation of mantle convection (Davies and Richards, 1992; Bercovici, 2003), the generation of plate tectonics from convective motions remains an elusive goal despite 30 years of research (e.g., Kaula, 1980; Hager and O'Connell, 1979, 1981; Ricard and Vigny, 1989; Vigny et al., 1991; Bercovici, 1993, 1995; Tackley, 1998, 2000b,c; Bercovici and Ricard, 2005; Landuyt et al., 2008; Landuyt and Bercovici, 2009a; van Heck and Tackley, 2008; Foley and Becker, 2009); see reviews by Bercovici et al. (2000); Gurnis et al. (2000); Tackley (2000a); Bercovici (2003).

Many models of plate generation from mantle convection adopt the "plasticity" formalism in which plate boundaries are developed instantaneously if convective stresses exceed a certain yield stress (e.g., Trompert and Hansen, 1998; Tackley, 2000b; Richards et al., 2001; Stein et al., 2004; van Heck and Tackley, 2008; Foley and Becker, 2009). This method, however, requires an unusually low yield-stress and, being an instantaneous mechanism, does not allow dormant plate boundaries that can be be re-activated, as is likely necessary for new subduction initiation in cold lithosphere (Gurnis et al., 2000; Toth and Gurnis, 1998; Lebrun et al., 2003; Hall et al., 2003). Moreover, laboratory experiments on rock deformation at moderate temperatures show much more complex behavior than simple plastic rheology (e.g., time-evolution of grain-size and texture, as well as interaction between different deformation mechanisms; see Karato, 2008).

The alternative damage model of plate generation predicts that plate boundaries develop from material damage leading to shear-localization and weakening, which survives for geologically extensive periods even after deformation ceases (Bercovici, 1998; Tackley, 2000c; Bercovici et al., 2001a,b; Auth et al., 2003; Bercovici and Ricard, 2003, 2005; Ricard and Bercovici, 2003, 2009; Landuyt et al., 2008; Landuyt and Bercovici, 2009a; Rozel et al., 2011). Observations of localized shear in mantle peridotitic mylonites (White et al., 1980; Etheridge and Wilkie, 1979; Jin et al., 1998; Furusho and Kanagawa, 1999) has prompted much activity in exploring grain-size shear-localizing feedback mechanisms (e.g., Kameyama et al., 1997; Braun et al., 1999; Montési and Hirth, 2003). In this case, a self-weakening positive feedback occurs because of the interaction of grain-size dependent rheologies (such as diffusion creep or grain-boundary sliding; see Hirth and Kohlstedt (2003)) and grain-reduction driven by deformation through dynamic recrystallization (e.g., Karato et al., 1980; Urai et al., 1986; Derby and Ashby, 1987; Doherty et al., 1997; Shimizu, 1998; Lee et al., 2002). However, this localizing feedback mechanism is paradoxical because grain-reduction by recrystallization is generally thought to occur only in dislocation creep, which is independent of grain-size, while rheological softening by grain-reduction only occurs in diffusion creep, when the grains cannot be reduced (Etheridge and Wilkie, 1979; Karato and Wu, 1993; De Bresser et al., 1998, 2001). In principle, the boundary between diffusion and dislocation creep is a stable equilibrium state for grain evolution (i.e, large grains in dislocation creep and small grains in diffusion creep respectively shrink and grow toward this state), hence the rheology tends to become anchored closed to this boundary on the piezometric curve. Near the boundary, complex interactions can ensue, leading to effective rheologies that are dependent on both grain-size and stress. Such interactions can either be due to mixing of creep mechanisms over grain-size distributions that span the boundary (e.g., Rozel et al., 2011), or to unique mechanisms like grain-boundary sliding (e.g., see Hirth and Kohlstedt, 2003; Hansen et al., 2012). These effects are not necessarily distinguishable in that both mixing and grain-boundary sliding lead to similar grain-size dependence (which is weaker than for diffusion creep), and stress dependence (which is slightly stronger than for dislocation creep) (see Rozel et al., 2011; Hansen et al., 2012). Nevertheless, these interactions are bound close to the diffusion-dislocation boundary where grain-reduction and thus localization feedbacks are restricted (Rozel et al., 2011). In addition, grain-growth and healing of weak zones in single mineral or single-phase systems is quite fast (Karato, 1989), which would cause fine-grained weak zones in the lower lithosphere to vanish in less than a million years (see Bercovici and Ricard, 2012).

However, actual lithospheric rocks are at least two-phase or polycrystalline materials (e.g., peridotite, which is roughly 60% olivine and 40% pyroxene). Secondary phases are well known to impede grain-growth by Zener pinning (e.g., Smith, 1948; Hillert, 1988; Solomatov et al., 2002) and can interact with deformation mechanisms by holding grain-size in the diffusion creep regime, thus stabilizing shear zones (Olgaard, 1990; Warren and Hirth, 2006; Mehl and Hirth, 2008; Herwegh et al., 2011; Linckens et al., 2011). In Bercovici and Ricard (2012) we proposed a new mechanism of grain-damage combined with Zener pinning that drives weakening and localization, and over-comes the problems with single-phase grain-reduction models. In particular, damage to the interface between phases increases the concentration of ever smaller pinning surfaces, which not only prevent grain-growth but even reduce grain-size while still in the diffusion creep regime. Damage combined with pinning thus allows a positive feedback between grain reduction and diffusion-creep weakening in deformation zones, thus promoting localization. Moreover, grain growth and weak-zone healing are greatly impeded by enhanced Zener pinning, thus leading to long-lived relic weak zones.

In this paper we apply the model of Bercovici and Ricard (2012) to some simple multi-dimension flow calculations to test the efficacy of the model in generating toroidal (strike-slip) flow from a convective type poloidal (divergent-convergent) flow field. Toroidal motion is one of the key metrics of plate generation theory and it can only be obtained in strongly non-linear rheological feedback mechanisms (see Bercovici, 2003). The simple flow field involves source-sink flow in a horizontal plane akin to a ridge-subduction system in the lithosphere. This imposed flow is applied to a fluid layer with our grain-damage mechanism and the toroidal strike-slip field is analyzed for its plate-like properties. Moreover, we use the source-sink model to impose a rapid change in plate-driving forces and examine the effect of

relic damage zones (as pseudo-plate boundaries) on plate evolution.

2. Source-Sink Model with Grain and Interface Damage and Pinning

Our model continuum has two phases of comparable (though not identical) density, viscosity and other properties, which are combined into a non-dilute mixture (e.g., 60%-40% mixture by volume, such as a mantle peridotite with olivine and pyroxene). The phases each have unique grain-size distributions with mean grain-sizes $\mathcal{R}_i$ (where i denotes the primary or secondary phase, i.e., $i = 1$ or 2), which evolve separately. Furthermore, the phases are separated by an interface that we assume to be isotropic and is thus described by a scalar interface density α, which represents the interfacial area per unit volume of the mixture (Bercovici et al., 2001a). This interface density can be directly associated with an interface curvature, and in particular a characteristic radius of curvature, or "roughness", of the interface r.

Finally, Zener pinning occurs if a grain, of either phase, is growing and the migration of its boundary is obstructed by the interface with the other phase (where this interface is, for example, the contact between olivine and pyroxene grains); the interface density thus represents the concentration of obstructing boundaries and similarly the interface curvature controls the effectiveness of the resulting pinning.

The primary goal of this paper is to study the classic plate-mantle coupling problem of how well a convective poloidal flow field can generate toroidal flow through nonlinear rheological mechanisms (see reviews by Bercovici et al., 2000; Bercovici, 2003). In this analysis we prescribe a poloidal flow by imposing a source-sink field in a shallow-layer of fluid, nominally the lithosphere overlying a less viscous mantle (Bercovici, 1993, 1995, 1998; Bercovici and Ricard, 2005). In effect, the source-sink field represents vertical motion of underlying fluid being injected into or ejected from the horizontal shallow layer. This source-sink flow is then used to examine how our damage theory generates plate-like strike-slip shear or toroidal flow.

2.1. *Mass conservation and source-sink kinematics*

Conservation of mass in two-phase continuum mechanics dictates a relation for the volume fraction ϕ_i of phase i (i.e., either phase), which, assuming both phases are incompressible and there is no mass exchange between phases, leads to

$$\frac{\partial \phi_i}{\partial t} + \boldsymbol{\nabla} \cdot (\phi_i \mathbf{v}_i) = 0 \tag{1}$$

where $\mathbf{v}_i$ is the velocity of phase i. However, both phases are highly viscous and tightly coupled silicates with negligible relative motion (i.e., they do not separate or percolate through each other), thus we assume both have the same velocity at a given point in space (i.e., in a small control volume in space) such that $\mathbf{v}_i = \mathbf{v}$. Summing (1) over i and noting that $\sum_i \phi_i = 1$, we arrive at

$$\boldsymbol{\nabla} \cdot \mathbf{v} = 0 \tag{2}$$

which implies that

$$\frac{D\phi_i}{Dt} = 0 \tag{3}$$

where $D/Dt = \partial/\partial t + \mathbf{v} \cdot \boldsymbol{\nabla}$ is the material derivative. Thus if ϕ_i is initially uniform (as assumed below, in the application of this model) it will remain so indefinitely.

The thin layer with which we model flow is assumed to be bounded above and below by inviscid half-spaces (i.e., the ocean and atmosphere above, the low-viscosity asthenosphere below) and thus has free-slip boundaries. The components of velocity are given by

$$\mathbf{v} = u\hat{\mathbf{x}} + v\hat{\mathbf{y}} + w\hat{\mathbf{z}} \tag{4}$$

Within the layer we assume vertical flow w is negligible, and thus the free-slip boundaries leads to the condition that $\partial u/\partial z = \partial v/\partial z = 0$ on the top and bottom of the layer. We further assume that the layer is so thin that this condition exists across the entire width of the layer, and thus u and v are independent of z.

In general, a solenoidal velocity field that satisfies (2) is

$$\mathbf{v} = \boldsymbol{\nabla} \times (\psi\hat{\mathbf{z}}) + \boldsymbol{\nabla} \times \boldsymbol{\nabla} \times (\theta z\hat{\mathbf{z}}) \tag{5}$$

where ψ is the toroidal stream function and θ is the poloidal potential, and both are functions of x, y and time t only. The velocity given by (5) can be rewritten as

$$\mathbf{v}_H = \boldsymbol{\nabla}\theta + \boldsymbol{\nabla} \times (\psi\hat{\mathbf{z}}) \;\text{ and }\; w = -z\nabla^2\theta \tag{6}$$

where $\mathbf{v}_H = (u, v, 0)$, is the horizontal velocity vector.

We are only concerned with lateral flow in the thin horizontal fluid layer that is driven by an imposed source-sink field, which represents injection and ejection of material from below. We define the thin layer to exist near $z = 0$ such that, according to (6), w is negligibly small, although $\partial w/\partial z$ is not. Indeed, the negative of $\partial w/\partial z$ represents the net vertical volume flux per unit volume (or at a point) of material being injected into the thin layer (i.e., if the layer has thickness h, then the net vertical volume flux over an infinitesimal area is $[w(z = 0) - w(z = h)]dxdy \approx -(\partial w/\partial z)hdxdy$). We therefore prescribe the source-sink field (due to vertical injection/ejection) as $S = -\partial w/\partial z$, which, using (6), can be restated in terms of the poloidal field as

$$\nabla^2\theta = S \quad . \tag{7}$$

Since the source-sink field S is prescribed, (7) is sufficient to determine the potential θ.

One of the key metrics of plate-like motion is focused toroidal motion in the form of concentrated bands of vertical vorticity that, if they were to represent a truely discontinuous strike-slip fault, would by line singularities. Vertical vorticity is defined as $\Omega = \hat{\mathbf{z}} \cdot \boldsymbol{\nabla} \times \mathbf{v}$ and represents the rate of strike-slip shear. Given

(6) the vorticity and toroidal potential are related by

$$\nabla^2\psi = -\Omega \tag{8}$$

However, Ω itself is determined by the momentum equation which we treat next.

2.2. *Source-sink dynamics*

The conservation of momentum in creeping two-phase flow with grained phases was prescribed by Bercovici and Ricard (2012) and, in the limit where the two phase velocities are the same (i.e., $\mathbf{v}_i = \mathbf{v}$), the summed momentum equation is sufficient and is given by

$$0 = \boldsymbol{\nabla}\bar{\Pi} + \boldsymbol{\nabla}\cdot\underline{\bar{\boldsymbol{\tau}}} + \bar{\rho}\mathbf{g} + \boldsymbol{\nabla}(\gamma_{\rm I}\alpha) \tag{9}$$

where the pressure Π, stress $\underline{\boldsymbol{\tau}}$ and density ρ are volume averaged over the two phases (i.e., for any quantity q, $\bar{q} = \sum_i \phi_i q_i$); $\mathbf{g}$ is gravitational acceleration; $\gamma_{\rm I}$ is the surface tension on the interface between phases; and α is the interface density (interface area per unit volume). The internal pressure on phase i, Π_i, includes the effect of surface tension on the grain boundaries (Ricard and Bercovici, 2009; Bercovici and Ricard, 2012). Finally, since the two phases have the same solenoidal velocity, the volume averaged stress tensor is

$$\underline{\bar{\boldsymbol{\tau}}} = \bar{\mu}\left(\boldsymbol{\nabla}\mathbf{v} + [\boldsymbol{\nabla}\mathbf{v}]^{\rm t}\right) \tag{10}$$

where $\bar{\mu}$ is the volume average of the viscosities μ_i, the rheological model of which will be discussed below in §2.3.

Substituting (10) into (9) and taking $\hat{\mathbf{z}}\cdot\boldsymbol{\nabla}\times$ of the resulting equation leads to an elliptic equation for the vorticity Ω

$$\begin{aligned}\bar{\mu}\nabla^2\Omega = &-2\boldsymbol{\nabla}\bar{\mu}\cdot\boldsymbol{\nabla}\Omega - \hat{\mathbf{z}}\cdot\boldsymbol{\nabla}\bar{\mu}\times\boldsymbol{\nabla}S \\ &+ \Delta^*\bar{\mu}\left(\Delta^*\psi - 2\frac{\partial^2\theta}{\partial x\partial y}\right) + 2\frac{\partial^2\bar{\mu}}{\partial x\partial y}\left(\Delta^*\theta + 2\frac{\partial^2\psi}{\partial x\partial y}\right)\end{aligned} \tag{11}$$

where we define the differential operator $\Delta^* = \partial^2/\partial x^2 - \partial^2/\partial y^2$ (Bercovici, 1993). A non-zero vorticity depends on forcing from the source-sink field S through gradients in the viscosity. Viscosity variability is dictated by the rheological model for the medium, which is discussed in the next section.

2.3. *Rheology*

As described in Bercovici and Ricard (2012), a material parcel (i.e., small control volume) has two phases, each of which has a non-uniform grain-size distribution; grains in these distributions will predominantly undergo either diffusion or dislocation creep depending on whether they are, respectively, smaller or bigger than a critical size defining the transition between creep mechanisms (e.g., see Rozel et al., 2011; Bercovici and Ricard, 2012, Appendix F.7). The strain-rate tensor of either phase averaged over the grain-size distribution reflects a mixture, or composite, of creep mechanisms, and is given by

$$\underline{\dot{\boldsymbol{\epsilon}}} = \tfrac{1}{2}(\boldsymbol{\nabla}\mathbf{v} + [\boldsymbol{\nabla}\mathbf{v}]^{\rm t}) = \left(a_i\tau_i^{n-1} + \frac{b_i}{\mathcal{R}_i^m}\right)\underline{\boldsymbol{\tau}}_i \tag{12}$$

assuming that stress is the same for all grains of like phase in the parcel; note that while the averaged strain-rate is the same for both phases in the parcel (since they have the same macroscopic velocity), their stresses can differ. In (12), $\tau_i^2 = \frac{1}{2}\underline{\boldsymbol{\tau}}_i : \underline{\boldsymbol{\tau}}_i$ is the second stress invariant for phase i, $\mathcal{R}_i$ is the characteristic or mean grain-size for phase i, a_i is the dislocation creep compliance for phase i, n is the power-law index (typically $n = 3$), and m is an exponent that is typically 2 for diffusion through grains (Nabarro-Herring creep) and 3 for diffusion along grain boundaries (Coble creep); the exponents n and m are assumed the same for both phases for simplicity although that assumption is easily relaxed. Assuming log-normal grain distribution with dimensionless variance σ for each phase, the macroscopic diffusion-creep compliance compliance b_i depends on both the grain-scale compliance B_i and the shape of the grain-size distribution according to

$$b_i = \frac{\lambda_{3-m}}{\lambda_3}B_i \quad \text{where} \quad \lambda_n = e^{n^2\sigma^2/2}. \tag{13}$$

(see Rozel et al., 2011). In general, the development of macroscopic relations from microscopic (i.e., grain-scale) properties involves averaging over moments of the grain-size distribution, which invariably introduces normalization factors like λ_n (see Ricard and Bercovici, 2009; Rozel et al., 2011; Bercovici and Ricard, 2012). We choose $\sigma = 0.8$, which allows a typical dimensional variance of order $\mathcal{R}_i$ (Bercovici and Ricard, 2012). The composite rheology (12) implies that the transition from dislocation to diffusion creep occurs for the macroscopic parcel at a critical grainsize $\mathcal{R}_c = [b_i/(a_i\tau_i^{n-1})]^{1/m}$; thus, a parcel whose grain-size distribution has a mean size far from this critical value will be predominantly in one creep mechanism or the other, while a mean grain-size exactly at this value has roughly half its grains in diffusion creep and the other half in dislocation creep, depending on the precise distribution shape (see also De Bresser et al., 1998). The viscosity of phase i is defined by (see (12))

$$\mu_i = \frac{1}{2}\left(a_i\tau_i^{n-1} + \frac{b_i}{\mathcal{R}_i^m}\right)^{-1} \tag{14}$$

in which τ_i is the solution to

$$a_i\tau_i^n + \frac{b_i}{\mathcal{R}_i^m}\tau_i - \dot{e} = 0 \tag{15}$$

for a given $\dot{e}$, where

$$\begin{aligned}\dot{e}^2 = \tfrac{1}{2}\underline{\dot{\boldsymbol{\epsilon}}} : \underline{\dot{\boldsymbol{\epsilon}}} = &\left(\frac{\partial^2\theta}{\partial x^2}\right)^2 + \left(\frac{\partial^2\theta}{\partial y^2}\right)^2 + \left(\frac{\partial^2\theta}{\partial x\partial y}\right)^2 + \frac{\partial^2\theta}{\partial x^2}\frac{\partial^2\theta}{\partial y^2} \\ &+ \left(\frac{\partial^2\psi}{\partial x\partial y}\right)^2 + \frac{1}{4}(\Delta^*\psi)^2 + \frac{\partial^2\psi}{\partial x\partial y}\Delta^*\theta - \frac{\partial^2\theta}{\partial x\partial y}\Delta^*\psi\end{aligned} \tag{16}$$

provided the velocity field (6). Equation (15) can be solved exactly (for $n = 2$ or $n = 3$) or implicitly for $\tau_i(\dot{e})$ (e.g., see Bercovici and Ricard, 2012, §4.1). The viscosity thus depends on the second strain-rate invariant $\dot{e}^2$, the grain-size $\mathcal{R}_i$ in phase i, which evolves and varies according to deformation, damage and Zener pinning, as discussed in the next section.

2.4. *Grain and interface evolution and pinning*

The mean grain-size $\mathcal{R}_i$ of phase i evolves through the competition between surface-tension driven coarsening (i.e., normal grain growth) and damage. Damage to grains is described macroscopically in terms of the deformational work used to create surface energy on grain boundaries, while microscopically this occurs through mechanisms such as dynamic recrystallization.

However, grain growth and damage is also affected by blocking surfaces imposed by the interface between the two different phases (e.g., the contact between olivine and pyroxene grains), the classic manifestation of which is Zener pinning. The interface blocks grain-boundary migration and the more curved the interface the more it causes grain-boundary distortion, which can impede and even reverse grain-growth and make grains more susceptible to damage (Bercovici and Ricard, 2012). The interface is represented here by the interface density (interface area per unit volume) α, which we prescribe to be a function of both volume fraction of the phases ϕ_i and the interface radius of curvature r

$$\alpha = \eta(\Phi)/r \tag{17}$$

where $\Phi = \prod_i \phi_i$ and η is a function depending on mixture morphology, but necessarily goes to 0 as either phase fraction $\phi_i \to 0$ (Bercovici and Ricard, 2005, 2012); however, in general, for simple morphologies, $\eta \approx 3\Phi$ (Bercovici and Ricard, 2012). The interface curvature itself evolves, both by coarsening (i.e., smoothing of the interface, as well as growth and merging of grains) as well as damage via deformation, distortion and/or rending of the interface. As shown by Bercovici and Ricard (2012) the evolution of the grain-size and interface roughness equations are similar and appear as

$$\frac{D\mathcal{R}_i}{Dt} = \frac{G_i}{p\mathcal{R}_i^{p-1}}\mathcal{Z}_i - \frac{\lambda_3}{\lambda_2}\frac{\mathcal{R}_i^2}{3\gamma_i}\mathfrak{f}_G(1-\mathfrak{f}_I)\Psi_i\mathcal{Z}_i^{-1} \tag{18}$$

$$\frac{Dr}{Dt} = \frac{\eta G_1}{qr^{q-1}} - \frac{r^2}{\eta\gamma_1}\mathfrak{f}_I\overline{\Psi} \tag{19}$$

where G_i and G_I are coarsening coefficients for the grain boundaries and interface, respectively, p and q are exponents (typically $p = 2$ and $2 \le q \le 4$), γ_i is the grain-boundary surface energy (i.e., the surface energy at the contact between like grains of phase i), γ_1 is, as defined already, the surface energy at the interface between phases (i.e., between grains of different phases), $\mathfrak{f}_I$ is the partitioning fraction governing how much deformational work goes toward creating interface surface energy, while $\mathfrak{f}_G$ is the fraction of remaining work going toward creating grain-boundary energy. The deformational work in phase i is given by $\Psi_i = \underline{\boldsymbol{\tau}}_i : \underline{\dot{\mathbf{e}}} = 2\mu_i\underline{\dot{\mathbf{e}}} : \underline{\dot{\mathbf{e}}} = 4\mu_i\dot{e}^2$ and the volume averaged work is $\overline{\Psi} = \sum_i \phi_i\Psi_i$. The interface blocking of grain growth is given by the Zener pinning factor

$$\mathcal{Z}_i = 1 - \mathfrak{c}(1-\phi_i)\frac{\mathcal{R}_i^2}{r^2} \quad \text{where} \quad \mathfrak{c} = \frac{3\lambda_4}{160\lambda_2} \tag{20}$$

(see Bercovici and Ricard, 2012). The Zener pinning effect acts to slow down and even reverse grain growth as r becomes comparable to or smaller than $\sqrt{\mathfrak{c}(1-\phi_i)}\mathcal{R}_i$. Likewise it facilitates grain damage by reducing the energy contrast between large and small grains (i.e., it causes more distortion and higher effective grain boundary energy on large grains, thus breaking such grains into smaller less distorted grains takes less energy).

However, as stipulated by dynamic recrystallization theory, we also prescribe that damage to grains only occurs in the fraction of the medium that deforms by dislocation creep; as shown by (Rozel et al., 2011), this is accomplished by prescribing that $\mathfrak{f}_G\dot{e}_i = \mathfrak{f}_G^* a_i\tau_i^n$ or that the partitioning fraction is given by

$$\mathfrak{f}_G = \mathfrak{f}_G^*\left(1 + \frac{b_i}{a_i\mathcal{R}_i^m\tau_i^{n-1}}\right)^{-1} = \mathfrak{f}_G^*\left(1 + \left(\frac{\mathcal{R}_c}{\mathcal{R}_i}\right)^m\right)^{-1} = 2\mathfrak{f}_G^*\mu_i a_i\tau_i^{n-1} \tag{21}$$

where $\mathfrak{f}_G^*$ is the maximum possible value of $\mathfrak{f}_G$. Note that the stress is still determined as a mixture of diffusion and dislocation creep for an imposed total strain-rate, but the damage to grains only occurs for the part of the strain-rate undergoing dislocation creep.

Because of the limitation on grain damage through (21), damage is more effective at distorting and sharpening the interface, which then forces grain-size reduction by pinning (through the factor $\mathcal{Z}_i$), driving the medium into diffusion creep. In this way damage and self-weakening in the diffusion creep regime can co-exist, which is normally disallowed in single-phase minerals (since the creep mechanisms are exclusive, unless the system holds close to the diffusion-dislocation creep boundary).

2.5. *Dimensionless governing equations*

To begin with we assume that ϕ_i is uniform and constant and simply provides the mixture ratio for our two-phase model lithosphere (e.g., $\phi_2 = 60\%$ for olivine and $\phi_1 = 40\%$ pyroxene for a mantle-lithosphere peridotite). In this case $\eta \approx 3\phi_1\phi_2$ is also uniform and constant and we use both ϕ_i and η within the nondimensionalizing scales.

We use the amplitude of the source-sink field $\mathsf{S} = \max|S|$ for a rate scale (inverse of time), and the characteristic separation of the source and sink L as our macroscopic length scale. We nondimensionalize time according to $t = \mathsf{S}^{-1}t'$, spatial variables according to $(x, y, z) = \mathsf{L}(x', y', z')$, $\boldsymbol{\nabla} = \mathsf{L}^{-1}\boldsymbol{\nabla}'$, and the velocity, flow potentials, divergence, vorticity and strain-rate according to

$$(S, \Omega, \underline{\dot{\mathbf{e}}}, \mathbf{v}, \theta, \psi) = \mathsf{S}(S', \Omega', \underline{\dot{\mathbf{e}}}', \mathsf{L}\mathbf{v}', \mathsf{L}^2\theta', \mathsf{L}^2\psi') \tag{22}$$

We further define the stress, viscosity and grain-size scales ac-

cording to

$$\boldsymbol{\tau} = (\mathsf{S}/\bar{a})^{1/n} \quad , \quad \boldsymbol{\mu} = \boldsymbol{\tau}/\mathsf{S} \, , \quad \text{and} \quad \mathsf{R} = (\bar{b}\boldsymbol{\mu})^{1/m} \tag{23}$$

where $\bar{a} = \sum_i \phi_i a_i$ and $\bar{b} = \sum_i \phi_i b_i$; thus we nondimensionalize stress, viscosity grain-size and interface roughness according to $\underline{\boldsymbol{\tau}}_i = \boldsymbol{\tau}\underline{\boldsymbol{\tau}}'_i$, $\mu_i = \boldsymbol{\mu}\mu'_i$ and $(\mathcal{R}_i, r) = \mathsf{R}(\mathcal{R}'_i, r')$. With these scaling relationships, the dimensionless governing equations for flow are, after dropping the primes, unchanged from (6)–(8), and (11). Likewise the relations for the dimensionless viscosity μ_i, stress invariant τ_i, and strain-rate invariant $\dot{e}$ are the same as given by (14)–(16), except for replacing a_i with $\mathsf{a}_i = a_i/\bar{a}$, and b_i with $\mathsf{b}_i = b_i/\bar{b}$. In general we expect comparable rheologies between the two phases such that $a_1 \approx a_2$ and $b_1 \approx b_2$ in which case we can assume $\mathsf{a}_i \approx \mathsf{b}_i \approx 1$.

The dimensionless evolution equations for $\mathcal{R}_i$ and r become, after substituting in (21),

$$\frac{D\mathcal{R}_i^p}{Dt} = C_i\mathcal{Z}_i - \mathcal{D}_i\mathcal{R}_i^{p+1}\tfrac{1}{2}\mathsf{a}_i\tau_i^{n+1}\mathcal{Z}_i^{-1} \tag{24}$$

$$\frac{Dr^q}{Dt} = C_\mathrm{I} - \mathcal{D}_\mathrm{I} r^{q+1}\bar{\mu}\dot{e}^2 \tag{25}$$

where

$$C_i = \frac{G_i}{\mathsf{S}\mathsf{R}^p} \quad , \quad C_\mathrm{I} = \frac{\eta G_\mathrm{I}}{\mathsf{S}\mathsf{R}^q} \tag{26}$$

and

$$\mathcal{D}_i = \frac{4p\lambda_3 \mathfrak{f}_\mathrm{G}^*(1-\mathfrak{f}_\mathrm{I})\mathsf{R}\mathsf{S}^{1/n}}{3\lambda_2\gamma_i\bar{a}^{1/n}} \quad , \quad \mathcal{D}_\mathrm{I} = \frac{4q\mathfrak{f}_\mathrm{I}\mathsf{R}\mathsf{S}^{1/n}}{\eta\gamma_1\bar{a}^{1/n}} \tag{27}$$

and the relation for the Zener pinning factor $\mathcal{Z}_i$ does not change from (20); see also Table 1 for a summary of dimensionless variables and parameters.

2.5.1. *Scales and numbers*

We can estimate geometric, kinematic, rheological and grain-growth scales for typical tectonic settings and olivine properties listed by Rozel et al. (2011). For a tectonic speed of 5cm/yr and a plate-boundary width of 100km, the typical source-sink (divergence/convergence) scale is $\mathsf{S} \approx 1.6 \times 10^{-14}\mathrm{s}^{-1}$. For olivine at lower-lithosphere temperatures of $T = 1000$K, the stress scale is $\boldsymbol{\tau} \approx 900$MPa (which is same order of but a factor of 3-5 bigger than typical tectonic stresses) and the grain scale $\mathsf{R} \approx 50\mu$m. At the same conditions, $G_i \approx 5 \times 10^{-23}\mathrm{m}^p/\mathrm{s}$ for $p = 2$. Finally, surface energies γ_i and γ_1 are generally $O(1)\mathrm{J/m}^2$, and $\eta \approx 3\phi_1\phi_2$ (Bercovici and Ricard, 2012).

To constrain q and G_1, we use the synthetic peridotite grain-growth experiments of Hiraga et al. (2010). The experimental value of interface roughness $r = \tilde{r}$ can be determined from the laboratory grain-size measurements in the large-time "pinning limit" (i.e., the limit of $\mathcal{Z}_i \to 0$ wherein grain-growth tracks interface coarsening; see Bercovici and Ricard, 2012, eqn. 12), from which we also estimate the experimental interface coarsening rate $d\tilde{r}/dt$. Equation (19) without damage implies that $G_\mathrm{I} = \eta^{-1}q\tilde{r}^{q-1}d\tilde{r}/dt$, which is verified by the data provided $2 \le q \le 4$ (Bercovici and Ricard, 2012) (as also implied by numerical simulations of coarsening in two phases; see Solomatov et al., 2002). Comparing the value of G_I with any q, denoted by $G_\mathrm{I}^{(q)}$, to that with $q = p$ leads to

$$\frac{G_\mathrm{I}^{(q)}}{G_\mathrm{I}^{(p)}} = \frac{q}{p}\tilde{r}^{q-p} \tag{28}$$

where $G_\mathrm{I}^{(p)}$ has the same units as G_i. For experiments with peridotitic mixtures of $\phi_1 = 0.42$, the pinning limit is reached when $\tilde{r} \approx 1\mu$m. Therefore, we infer that $G_\mathrm{I}^{(q)}$ is given by (28) for $\tilde{r} = 1\mu$m, where, as also determined by Bercovici and Ricard (2012), $G_\mathrm{I}^{(p)} \approx G_i/250$ for $p = 2$ (see Bercovici and Ricard, 2012, Fig. 6). Thus, for example, for $p = 2$ and $q = 4$, $G_\mathrm{I} = 2(\mu\mathrm{m})^2 G_i/250$.

Given these properties we can estimate the governing dimensionless numbers. Although there are several dimensionless parameters, the key ones are C_i, C_I, $\mathcal{D}_i$ and $\mathcal{D}_\mathrm{I}$. Otherwise we assume $\mathsf{a}_i = \mathsf{b}_i = 1$, $m = 3$ for Coble diffusion creep, $n = 3$ for dislocation creep, $p = 2$ for normal grain coarsening, and $2 \le q \le 4$ for interface coarsening (hence we will explore the effect of varying q).

For the plate kinematic and olivine properties inferred above, we use the grain coarsening number $C_i \approx 1$, which is probably an upper bound (given the assumed high lithosphere temperature, modest plate speed and wide plate boundary width); however we leave this parameter as is to be conservative. For $q = p = 2$ and a peridotic mixture ($\phi_1 = 0.42$), $C_\mathrm{I}/C_i = \eta G_\mathrm{I}/G_i \approx 3 \times 10^{-3}$; however to be conservative we limit this interface coarsening number to be $C_\mathrm{I} = 10^{-2}$. Using (26) and (28) for cases with $q \ne p$ yields $C_\mathrm{I}^{(q)}/C_\mathrm{I}^{(p)} = q/p(\tilde{r}/\mathsf{R})^{q-p}$; therefore for $p = 2$, when we increase q from 2 to 4 with $\tilde{r}/\mathsf{R} = 1/50$, we must decrease C_I to approximately 10^{-5}.

The damage numbers $\mathcal{D}_i$ and $\mathcal{D}_\mathrm{I}$ can be very large depending on what one assumes for $\mathfrak{f}_\mathrm{G}$ and $\mathfrak{f}_\mathrm{I}$, and in general $\mathcal{D}_\mathrm{I} \approx \mathcal{D}_i$. For $\mathfrak{f}_\mathrm{G}, \mathfrak{f}_\mathrm{I}$ of order a few tens of a percent to unity, $\mathcal{D}_\mathrm{I}$ and $\mathcal{D}_i$ are as much as $O(10^5)$. However, to be conservative, we assume that $\mathfrak{f}_\mathrm{G}, \mathfrak{f}_\mathrm{I} \ll 1$ such that $1 < \mathcal{D}_i, \mathcal{D}_\mathrm{I} < O(100)$; e.g., for the parameters listed above, cases with $\mathcal{D}_i, \mathcal{D}_\mathrm{I} \approx 100$ corresponds to $\mathfrak{f}_\mathrm{G}, \mathfrak{f}_\mathrm{I} \approx 2 \times 10^{-4}$. This value is well in the range of the estimates for $\mathfrak{f}_\mathrm{G}$ by Rozel et al. (2011) for olivine (10^{-2}–10^{-4}), or by Austin and Evans (2007) for calcite ($O(10^{-4})$).

2.6. ***Solution method***

We use a simple spectral transform technique with fast Fourier transforms to solve the model equations, as described previously (Bercovici, 1993, 1995, 1998; Bercovici and Ricard, 2005); a spatial grid of 128 by 128 points provides sufficient resolution. We first impose a source-sink field S (see description in Fig. 2a), from which θ is determined with (7); both S and θ thence remain fixed throughout any calculation. Given an initial uniform grain-size field the viscosity fields can be determined from (14) (noting that (a_i, b_i) are replaced with $(\mathsf{a}_i, \mathsf{b}_i) \approx (1, 1)$), which, with S and

Variable	Definition	Reference Equation(s)
$\mathbf{v}$	velocity	(6)
S	source-sink field (divergence)	(7)
Ω	vertical vorticity (strike-slip shear)	(8)
r	interface roughness	(25)
$\mathcal{R}_i$	mean grain-size of phase i	(24)
$\bar{\mathcal{R}}$	volume averaged grain-size	$\sum_i \phi_i \mathcal{R}_i$
$\mathcal{Z}_i$	Zener pinning factor	(20)
μ_i	viscosity of phase i	(14)
$\bar{\mu}$	average viscosity	$\sum_i \phi_i \mu_i$
τ_i	square-root of 2nd stress invariant of phase i	(12), (15)
$\dot{e}$	square-root of 2nd strain-rate invariant	(12), (16)
C_Ω	vorticity correlation	(29)
Dimensionless parameter	**Definition**	**Reference Equation(s)**
C_i	grain coarsening rate	(26), $C_i = 1$
C_1	interface coarsening rate	(26)
$\mathcal{D}_i$	grain damage rate	(27)
$\mathcal{D}_1$	interface damage rate	(27)
n	dislocation creep stress exponent	(12), $n = 3$
m	diffusion creep grain-size exponent	(12), $m = 3$
p	grain coarsening exponent	(24), $p = 2$
q	interface coarsening exponent	(25)
ϕ_i	volume fraction of phase i	(1), $\phi_1 = 0.4$, $\phi_2 = 0.6$

Table 1: Table of variables and dimensionless parameters (as referenced in the figures)

θ, can be used to find the vorticity Ω from (11) – which must be solved iteratively to convergence – and hence ψ from (8). With ψ and θ one obtains velocity from (6), $\dot{e}$ from (16), and τ_i from (15), which are then used to update the grain-size $\mathcal{R}_i$ and interface roughness r from (24) and (25). The new grain-size $\mathcal{R}_i$ is then used in the viscosity relation to update Ω and so on. Because the dislocation creep viscosity is singular at zero strain-rate, we impose a minimum value $\dot{e}^2_{min}$ on the second strain-rate invariant; we find that $\dot{e}^2_{min} \leq 10^{-4}$ has no significant effect on the results.

Other than imposing S, the only other initial condition we adopt is that the initial mean grain-sizes are dimensionally all about 500μm, but with the major phase's mean grain-size $\mathcal{R}_2$ being somewhat larger than that for the minor phase $\mathcal{R}_1$ (as is often observed in the laboratory and field), and that the interface roughness r is similar to but slightly less than $\mathcal{R}_1$ (as inferred from experiments; see Bercovici and Ricard, 2012, §3). Therefore, the dimensionless grain-size fields begin uniformly with $\mathcal{R}_1 = 8$ and $\mathcal{R}_2 = 12$ and the interface roughness is $r = 7.5$ (these values are also consistent with the range of values predicted for the quasi-steady pinning limit of $\mathcal{Z}_i \to 0$, where $\mathcal{Z}_i$ is given by (20)). A few comparison cases with both smaller and larger initial values of $\mathcal{R}_i$ and r were also run and their results are briefly summarized below (see §3.2.3).

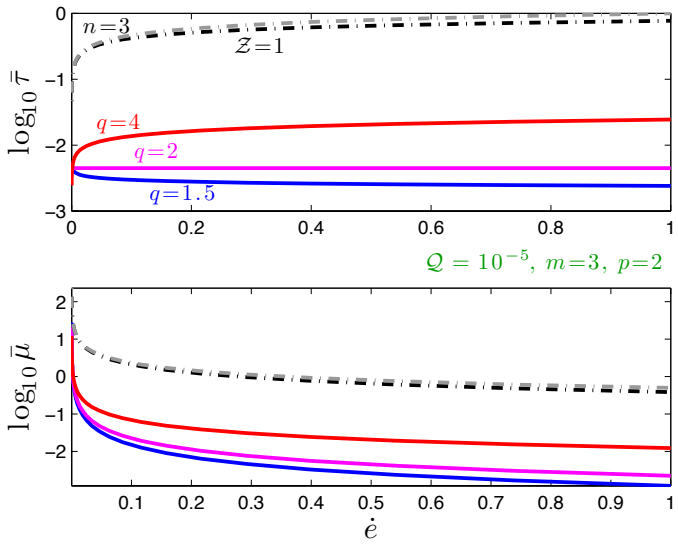

Figure 1: Effective rheology in simple shear from Bercovici and Ricard (2012) showing dislocation creep only with $n = 3$ (gray dash-dot), grain-damage without Zener pinning (black dash dot), and grain-damage with Zener pinning and 3 interface coarsening exponents $q = 1.5, 2, 4$ (colors, as indicated). The simple shear system has a different scaling law than employed in the source-sink system, thus some non-dimensional parameters are defined differently, as described in Bercovici and Ricard (2012). Nevertheless, Q is analogous to C_1 and is likewise much less than unity. All other parameters indicated have the same meaning as in this paper.

3. Results

3.1. *Effective rheology*

Bercovici and Ricard (2012) analyzed the system of grain-damage and pinning in steady-state one-dimensional uniform simple shear and inferred effective constitutive relations between imposed shear strain-rate and final steady-state stress (in particular, see Bercovici and Ricard, 2012, §4.2). We can apply the same method here to compare various non-Newtonian rheologies (Fig. 1). The standard dislocation-creep rheology (Fig. 1, gray dashed curves) provides a baseline for comparison since it is independent of grain-size; even though moderate damage does drive grain reduction, the grain-size evolution has no effect on the rheology and any localization or weakening is due to the explicit dependence of viscosity on stress or strain-rate. Such a rheology is given by (12) or (15) with $b_i = 0$, in which a typical mantle power-law index is $n = 3$ (as used in Fig. 1; see also Table 1 for a summary of dimensionless variables and parameters). This rheology shows viscosity reduction with increasing strain-rate, but with relatively large stresses and viscosities and hence poor to modest weakening and localization (as inferred by Bercovici, 1993). The dislocation creep rheology represents an upper bound on stress (and viscosity) for the medium; other rheologies for which grain-damage provides additional weakening will appear as a lower bound, since stress reaches its minimum in the final steady-state 1-D shear zone (Bercovici and Ricard, 2012).

The case with a full composite rheology ($b_i \neq 0$) and grain-damage but no Zener pinning (i.e., fixing $\mathcal{Z}_i = 1$; see Fig. 1 black dashed curves) is analogous to the system studied by Rozel et al. (2011), and is possibly relevant to inferred grain-boundary sliding near the diffusion-dislocation creep boundary. Grain-damage proceeds while the material is in the dislocation creep regime of stress–grain-size space, but once grain-size reaches the diffusion creep regime, grain-damage and grain-reduction cease (see (21)), and grain-size stays close to the critical value $\mathcal{R}_c$ at the diffusion-dislocation boundary. Without Zener pinning, the damage to the interface and reduction in r has no effect on grain-size and hence no effect on the rheology. In this case the system is only slightly more effective at causing localization than the standard dislocation creep rheology.

Cases with composite rheology, grain-damage and Zener pinning can show dramatically more softening, provided that the interface healing rate is very slow, as is to be expected (i.e., since interface healing occurs through long distance diffusion across phases or along the interface, rather than short-distance diffusion across grain boundaries; see also §2.5.1). The interface coarsening power-law index q has significant influence on the strength of the 1-D shear zone, as discussed in Bercovici and Ricard (2012). In particular, for $q < m - 1$ the rheology is velocity weakening (stress drops with increasing strain-rate), for $q = m - 1$ it approaches a pure plasticity limit (stress becomes independent of strain-rate) and for $q > m - 1$ it appears as a pseudo-plastic or power-law type rheology (see Fig. 1 color curves). In all such cases, even for $q > m - 1$, the stress and viscosity are significantly lower than both the simple power-law and "no-Zener pinning" cases, since they involve the system being driven far into diffusion creep with small grains and hence low stress and viscosity. Hence, weakening co-exists with grain-size reduction because even when the system is in the diffusion creep regime, damage reduces the interface roughness r, which in turn drives down grain-size through Zener pinning.

Although these effective rheologies are for 1-D, uniform simple shear, they are useful for interpreting non-uniform, multi-dimensional, time-dependent flow results. In particular, the dislocation creep curve represents an upper bound on strength and is associated with large grains, while the other effective rheological curves represent lower bounds and are associated with a minimum steady-state grain-size. Thus, for a given strain-rate, and provided the existence of some grain-damage, the grain-size will shrink and the stress will drop from the dislocation curve to one of the lower-bound curves, leading to classical localization behavior (i.e., a stress drop with increasing strain). Alternatively, for a given stress, large-grained regions on the dislocation creep curve have the smallest strain-rate, while small-grained regions on one of the other curves have the largest strain-rate; large differences in strain-rates for a given stress are also associated with localization. In the no-Zener-pinning case, there is little difference between the upper and lower stress bounds, and hence weak localization. For cases with Zener pinning, the difference between upper and lower stress bounds is large, hence localization is potentially significant. Such localization is evident in the source-sink calculations discussed next.

3.2. *Stationary source-sink flow*

We examine shear localization and toroidal flow generation in source-sink flow for several non-Newtonian rheological mechanisms as discussed above in §3.1. In particular we step through levels of complexity going from pure steady-state dislocation creep power law rheology (with $b_i = 0$ and $n = 3$), to grain-damage without Zener pinning (i.e., fixing $\mathcal{Z}_i = 1$), and finally to the general case of grain-damage with Zener pinning (see Table 1 for a summary of dimensionless variables and parameters).

In each case we hold the grain-coarsening parameter fixed to $C_i = 1$, which is on the higher end of its likely range, but is thus conservative in that it mitigates damage with faster healing. We examine the non-dimensional 2-D fields for Ω and $\mathbf{v}$ driven by the source-sink field S, in addition to the resulting interface roughness (or radius of curvature) field r, average grain-size $\bar{\mathcal{R}} = \sum_i \phi_i \mathcal{R}_i$, and mixture viscosity $\bar{\mu} = \sum_i \phi_i \mu_i$.

In all cases we display Ω with the same contour scale in which S is shown, in order to display the strength of the strike-slip vorticity relative to the driving source-sink field; values of Ω that exceed this scale saturate with a uniform color. For ideal plate-like flow, the vorticity would be $\widetilde{\Omega}$, which is a replica of S but rotated 90° clock-wise (Bercovici, 1993; Bercovici and Ricard, 2005). The measure of how well the produced vorticity Ω matches the

ideal vorticity $\widetilde{\Omega}$ is given by the correlation

$$C_\Omega = \frac{\int_A \Omega\widetilde{\Omega} dA}{\int_A \widetilde{\Omega}\widetilde{\Omega} dA} \tag{29}$$

where $dA = dxdy$ and A is the domain of the calculation. The vorticity correlation C_Ω is unity if the vorticity fields are identical, 0 if they are 90° out of phase and approaches −1 if they are 180° out of phase.

The relevant magnitudes of these fields are also determined as functions of time in order to track their evolution. The minimum values of r and $\mathcal{R}_i$ are of most importance for the material fields since they indicate the damage done to the interface and grains in deformation zones. The maximum vorticity and the vorticity correlation C_Ω are also tracked to show the evolution toward plate-like flow. The idealized vorticity $\widetilde{\Omega}$ has an amplitude of ±1; thus a produced vorticity maximum $\Omega_{\max}$ approaching or exceeding 1 is characteristic of being plate-like, at least in magnitude. A correlation C_Ω approaching 1 is indicative of plate-like structure as well as amplitude. The 2-D fields themselves are displayed toward the end of a calculation as the system reaches steady state.

3.2.1. Baseline case 1: Pure dislocation creep

The source-sink system with steady-state pure dislocation creep ($b_i = 0$, $\mathsf{a}_i = a_i/\bar{a} = 1$, and $n = 3$) provides a baseline comparison for all other calculations. As discussed by Bercovici (1993) a power-law rheology with index $n = 1$ is Newtonian, and this does not permit toroidal motion. A moderate mantle-like power law index of $n = 3$ is also known to generate only weak localization and toroidal motion, and much higher values of n make little added difference (Bercovici, 1993). Indeed, the source-sink model in this case (Fig. 2) produces relatively weak toroidal motion and un-plate-like flow wherein the velocity field appears predominantly dipolar (Fig 2a); moreover, the peak vorticity and vorticity correlation plateau quickly to modest values significantly less than 1 (Fig 2b). Although the grain-sizes $\mathcal{R}_i$ and interface roughness r are computed, they have no effect on the rheology and thus do not influence the flow field. In the end, weakening mechanisms must be considerably more effective in producing toroidal motion than a power-law of $n = 3$ to be considered viable plate-generating mechanisms.

3.2.2. Baseline case 2: Grain-damage without pinning

When grain-damage occurs without Zener pinning (by fixing $\mathcal{Z}_i = 1$), there is only grain reduction while the two phases deform via dislocation creep, i.e., at high stress and large grain-size. This case is equivalent to the single-phase system (Rozel et al., 2011) since there is no influence of one phase on the other through pinning.

In the source-sink driven model, damage without pinning provides modest toroidal motion and localization (Fig 3), only slightly better than the pure dislocation creep case. This result is to be expected since damage drives the initially large grain-sizes to the boundary between diffusion and dislocation creep, i.e., toward so-called piezometric equilibrium, after which grain-size stops evolving (Fig 3b); i.e., the diffusion-dislocation boundary delineates a stable equilibrium in grain-size, since grains grow if smaller than this size and shrink if larger (assuming damage is generating dislocations). Thus the composite rheology still has a large dislocation creep component to it. Note that while damage to the interface continues to drive the roughness r to smaller sizes, r itself has no influence on the system in this case. The maximum vorticity $\Omega_{\max}$ and vorticity correlation C_Ω peak with time and then approach a steady state value that is only modestly larger than the pure dislocation case, both significantly less than the idealized values of 1.

In short, without Zener pinning grain-damage cannot drive the grain-size completely out of the dislocation creep regime and thus the system retains a significant component of power-law dislocation-creep rheology. The rheology remains close to a power-law rheology with an exponent larger than for pure dislocation creep, and a weak grain size dependence (Rozel et al., 2011), similar to what is observed during grain-boundary sliding (e.g., Hirth and Kohlstedt, 2003; Hansen et al., 2012).

3.2.3. Grain-damage and pinning

When damage occurs with Zener pinning, the system can experience grain reduction even in the diffusion creep regime because damage to the interface and subsequent reduction in r drives grain reduction by Zener pinning. This system can attain significant localization and a very strong toroidal field, depending on the choice of parameters, especially the damage numbers $\mathcal{D}_\mathrm{I}$ and $\mathcal{D}_i$, which we set equal to each other for simplicity. The grain healing rate is fixed at $C_i = 1$, as mentioned above, and the interface healing rate is set to $C_\mathrm{I} = 10^{-2}$ for $q = 2$ and $C_\mathrm{I} = 10^{-5}$ for $q = 4$; we only consider these values of q since comparison to experiments implies they cover the most plausible range (Bercovici and Ricard, 2012).

For moderate values of $\mathcal{D}_\mathrm{I} = \mathcal{D}_i = 100$, highly plate-like localization and toroidal motion are readily obtained for both values of $q = 2$ and 4 and their associated C_I (Fig 4). The vorticity extrema in fact far exceed the idealized values of $\widetilde{\Omega}$ (indicated by the "saturated" peaks that appear as color bands in the vorticity field). Indeed $\Omega_{\max}$ reaches more than double the magnitude of $\widetilde{\Omega}$ and the correlation C_Ω readily reaches the idealized value of 1 (Figs. 4b,d). Hence the strike-slip shear bands dynamically reach much narrower structures than the imposed source and sink.

The material property fields also obtain plate-like characteristics. In particular, the viscosity fields display more contiguous narrow zones of weakness – akin to plate boundaries – than in either the cases with pure dislocation creep or with grain-damage sans pinning. Moreover, the minimum grain-sizes drop almost two orders of magnitude from their original values; the dimensional grain-sizes thus evolve from approximately 500μm to about 5μm, which is consistent with observations of grain-size distributions in mylonites (Warren and Hirth, 2006). The continuous weak zones are associated with regions undergoing more

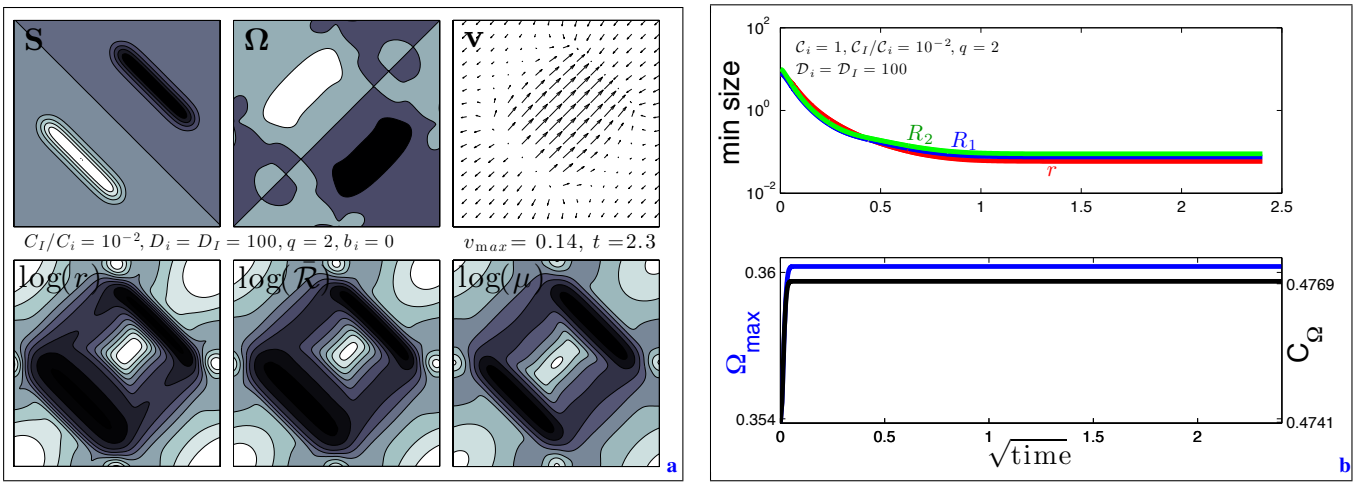

Figure 2: Source-sink driven flow and material fields. Frame (a) displays the imposed source-sink (divergence) field S, vorticity Ω (with the same contour interval as S), surface velocity field $\mathbf{v}$, interface roughness r, volume averaged mean grainsize $\bar{\mathcal{R}} = \sum_i \phi_i \mathcal{R}_i$, and volume averaged mean viscosity $\bar{\mu} = \sum_i \phi_i \mu_i$; the latter three quantities are shown in $\log_{10}$ for better resolution of minima. The dimensionless model domain is $-1 \le x, y \le +1$; the length of the source and sink as well as their separation distance are 1 (since the separation length is the nondimensionalizing length scale), while their half-width is 0.1, and amplitude is $|S|_{\max} = 1$ (since the dimensional amplitude of S is used for the strain-rate and inverse time scales). Frame (b) shows the time evolution of the minimum grainsizes $\mathcal{R}_i$ and interface curvature r, as well as the peak vorticity $\Omega_{\max}$ and correlation function C_Ω from (29). The case shown is for dislocation creep only (i.e., setting $b_i = 0$ in (12)-(15)) with $n = 3$. Contours are evenly spaced between extrema for each contour plot. The extrema for S are always ± 1. Extrema ([min,max]) in contour plots for Ω, r, $\bar{\mathcal{R}}$ and $\bar{\mu}$ are [-0.4,0.4], [0.06,3.9], [0.08,3.3] and [0.5,10.8], respectively

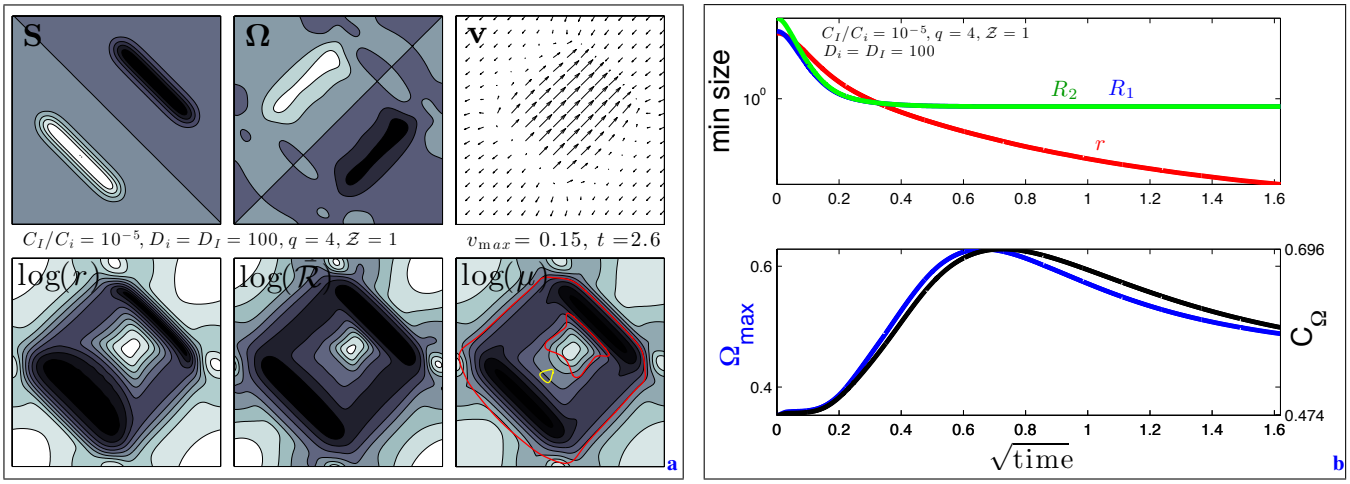

Figure 3: Same as Fig. 2 but with grain-damage and no Zener pinning. The case shown has an interface growth exponent of $q = 4$, but this only affects interface evolution and not the rheology or localization, since without pinning there is no coupling between interface and grains. Extrema ([min,max]) in contour plots for Ω, r, $\bar{\mathcal{R}}$ and $\bar{\mu}$ are [-0.5,0.5], [0.07,5.0], [0.8,4.6] and [0.2, 10.0], respectively. The viscosity field also displays color contours indicating fraction of compliance or deformation occuring in diffusion creep, given by $\bar{\mu}/[\sum_i \phi_i \mathcal{R}_i^m/(2b_i)]$; in particular regions between the red contours are more than 75% in diffusion creep and regions inside the yellow contour are more than 99% in diffusion creep, although in this case the lowest viscosity regions have a significant contribution from dislocation creep hence diffusion creep is only 99% dominant in a small island offset from the viscosity minima.

than 99% diffusion creep, i.e., where the grain-size distribution has been driven almost completely into the diffusion creep regime (see Figs 4a,c).

Obviously the damage number $\mathcal{D}_{\rm I}$ (and $\mathcal{D}_i$) influences the plate-like behavior. The values of $\Omega_{\max}$ and C_Ω as a function of $\mathcal{D}_{\rm I}$ can be determined from a suite of source-sink calculations (Fig. 5) and these demonstrate a very dramatic increase in plate-like toroidal motion with increasing damage number. For $\mathcal{D}_{\rm I} \sim O(1)$ the toroidal motion is weak and comparable to the pure dislocation case as expected, but for $\mathcal{D}_{\rm I} \sim O(10)$, the peak vorticity $\Omega_{\max}$ and correlation C_Ω approach idealized values of unity. For $\mathcal{D}_{\rm I} \sim O(100)$ the peak vorticity $\Omega_{\max}$ well exceeds, by factors of 2 and 3, the idealized values and the correlation C_Ω firmly saturates at 1. Since the maximum velocity changes only

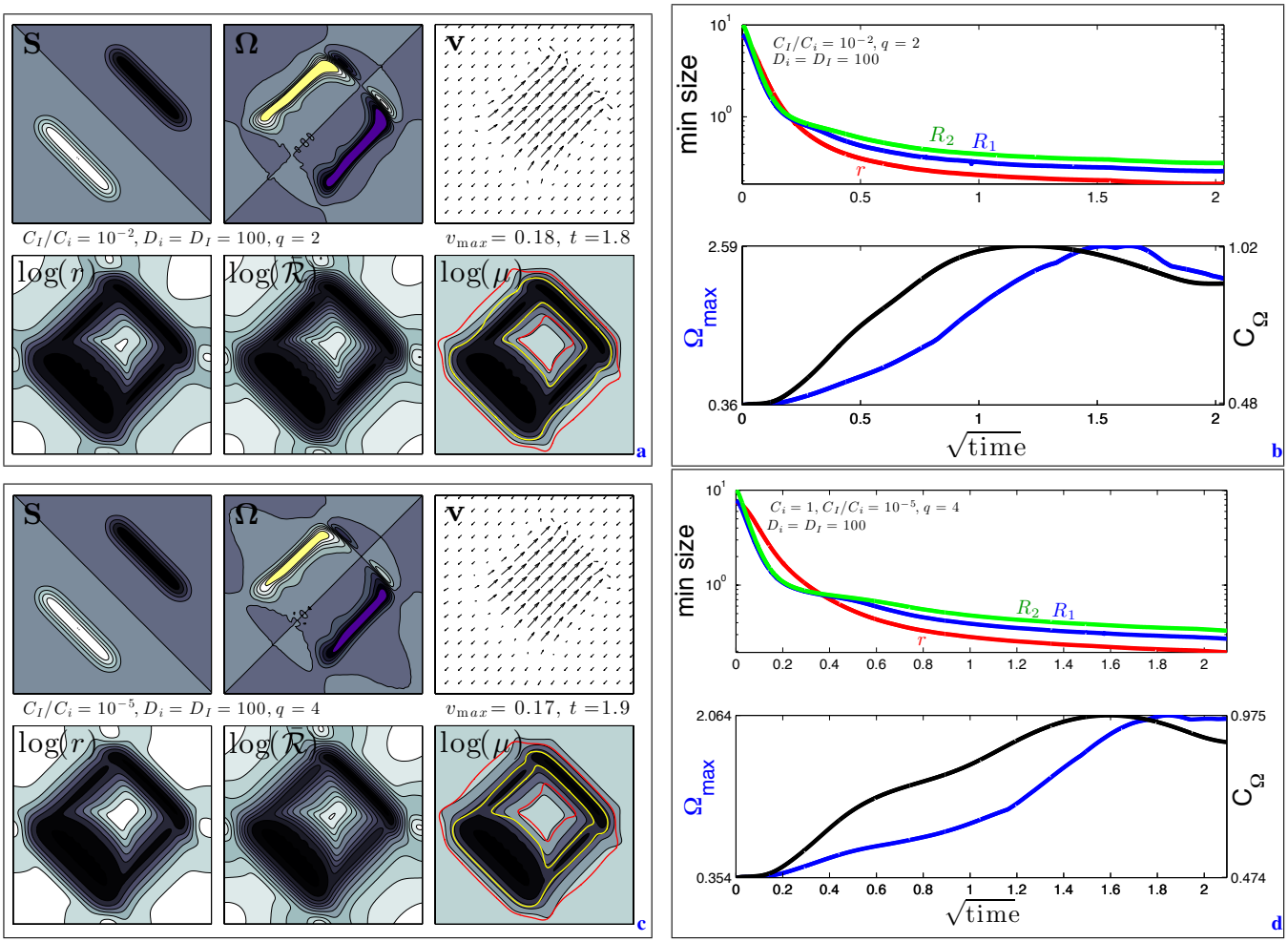

Figure 4: Same as Fig. 2 but with grain-damage and Zener pinning for two different cases with different interface coarsening exponents q as indicated. Extrema ([min,max]) in contour plots for Ω, r, $\bar{\mathcal{R}}$ and $\bar{\mu}$ are (a) [-2.4,2.4], [0.2,4.4], [0.3,4.1] and [0.02,9.6], respectively; and (c) [-1.5,1.5], [0.2,5.5], [0.4,4.3] and [0.03,9.8], respectively. Because contours in Ω have the same intervals as with S, the maximum and minimum values are saturated beyond ± 1 with yellow and indigo, respectively. As with the viscosity field in Fig.3, regions between the red contours are more than 75% in diffusion creep and those between yellow contours are more than 99% in diffusion creep.

slightly between cases (e.g., note the velocity maxima in Figures 2–4), the large increase in $\Omega_{\max}$ with $\mathcal{D}_\mathrm{I}$ is largely due to narrowing of the strike-slip shear zone; i.e., when $\Omega_{\max} \approx 1$ the strike-slip zone is approximately as wide as the source or sink bands (as it would be for the idealized vorticity $\widetilde{\Omega}$), thus for $\mathcal{D}_\mathrm{I} \sim O(100)$ the strike-slip zone is 2-3 times narrower than the source-sink bands.

The greater localization and plate-like behavior in the cases with pinning and grain-damage is largely due to the great separation in bounding stress–strain-rate curves indicated in §3.1. For a given stress, regions with small grains well into the diffusion creep regime will have much higher strain-rates than regions with large grains undergoing dislocation creep; this very contrast allows for substantial localization, thus rapidly deforming plate boundaries and weakly deforming plate interiors. However, this effect also depends somewhat on the initial grain-size distribution, which determines how much of the domain is initially undergoing dislocation creep. Initial grain-sizes either an order of magnitude bigger or smaller than shown here tend to increase or decrease the peak vorticity $\Omega_{\max}$ by a factor of approximately 2, respectively. However, this range of initial grain-sizes leads to flows that span the range from sufficiently plate-like ($\Omega_{\max} \approx 1$) to highly plate like ($\Omega_{\max} \approx 3-4$).

3.3. *Plate re-organization and plate-boundary inheritance*

The features of instantaneous plate-like motion such as *plateness* (i.e., strong plate interiors and weak plate boundaries; see Weinstein and Olson, 1992) and toroidal motion are important metrics of plate generation models. However, dormancy and reactivation of weak fault zones and plate boundaries are also important features of plate tectonics. In particular the inheritance of long-lived but inactive weak zones are thought to be key for initiation of new subduction zones (Gurnis et al., 2000; Toth and Gurnis, 1998; Lebrun et al., 2003; Hall et al., 2003). Moreover,

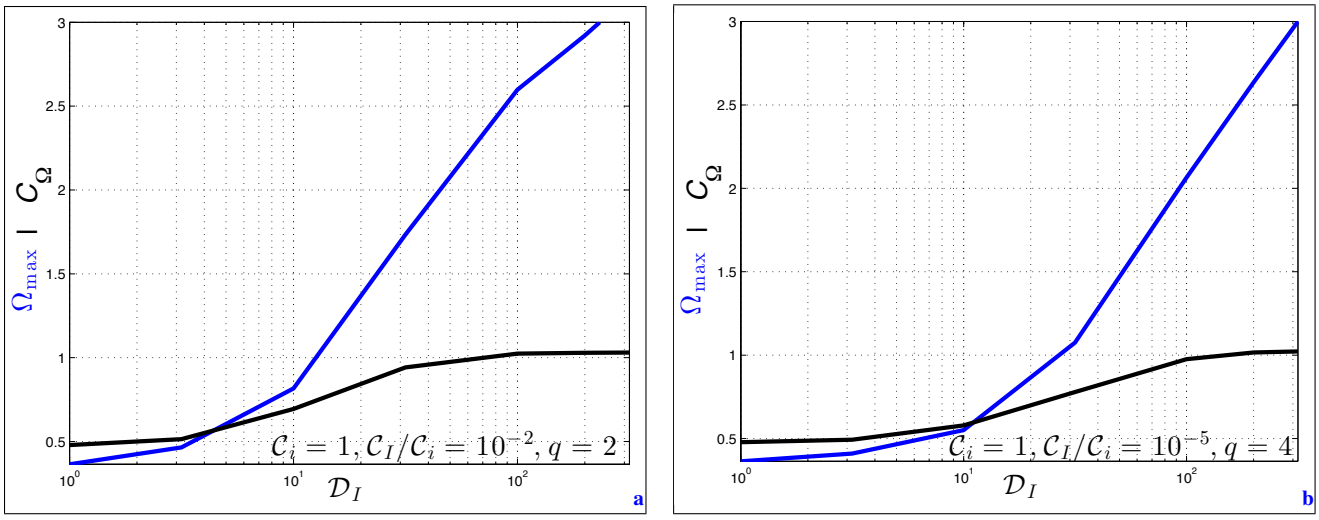

Figure 5: Maximum peak vorticity $\Omega_{\max}$ (blue) and correlation C_Ω (black) obtained versus the damage numbers $\mathcal{D}_I = \mathcal{D}_i$ in calculations with pinning and damage (as in Fig. 4) for two different cases with different interface coarsening exponents q as indicated.

changes in plate motion can also leave relic plate boundaries that are suboptimally aligned with the new plate direction, such as the San Andreas Fault system relative to the current direction of the Pacific plate. How a plate and plate boundaries evolve after a plate motion change are a key aspect of paleomagnetic plate reconstructions, which provide important constraints on plate generation theories. Indeed, one of the advantages of damage theory over an instantaneous rheology model for plate generation is that it allows dormant or inherited weak zones that can be misaligned with the current plate direction and thus influence plate evolution and geometry.

3.3.1. *Experimental set-up*

Here we explore one simple experiment on the effect of rapid plate motion change on plate boundary evolution, given some selected damage and healing parameters. The experiment is an abstraction of the change in motion of the Pacific plate associated with the 47Ma Emperor-Hawaiian bend (see Sharp and Clague, 2006). In particular we initiate calculations with the source-sink field driving motion 15° West of North (i.e, W15N or at an angle of 105° from the x axis, approximately the azimuth of the Emperor Seamount chain) for both sets of interface healing parameters used above (i.e., $(q, C_I) = (2, 10^{-2})$ and $(4, 10^{-5})$). The calculations are run until a plate-like vorticity field is well established with a peak value of $\Omega_{\max} \approx 1$, i.e., comparable to the ideal peak value of $\widetilde{\Omega}$ (Figs. 6a and 7a). The source-sink field is then abruptly rotated 45° counter-clockwise to a W60N direction, roughly the azimuth of the Hawaiian Ridge (Figs. 6b and 7b), which imposes a rapid change in so-called plate driving force (although the Earth's actual driving force derives from the mantle's buoyancy field, which has a direct correlation to poloidal flow). The vorticity field then evolves from its original well-established strike-slip type localizations that are orientated W15N, to its new configuration over a long time integration (Figs. 6b-e and 7b-e). The evolution of the minimum grain-size and interface roughness as well as vorticity characteristics $\Omega_{\max}$ and C_Ω are tracked through the entire experiment (Figs. 6f and 7f). The experiments are run with a high enough damage number to establish plate-like vorticity ($\mathcal{D}_I = 100$). The experiment with $q = 2, C_I = 10^{-2}$ (Fig. 6) has faster interface coarsening than the case with $q = 4, C_I = 10^{-5}$ (Fig. 7), which allows us to infer the effect of healing on plate reorganization and evolution.

3.3.2. *Evolution of strike-slip vorticity*

After the plate-motion change (i.e., the source-sink rotation), the vorticity field retains "memory" of the original plate configuration throughout the experiment, and does not reach a regular square plate-like structure (as in the simpler static-source-sink experiments of §3.2), although the experiment with faster healing progresses slightly further to regular strike-slip type margins. After the abrupt rotation, the peak vorticity $\Omega_{\max}$ drops slightly but then continues to increase to values as large as in the static source-sink experiments (Figs. 6f and 7f). However, the vorticity correlation C_Ω drops significantly immediately after the rotation as expected, since the geometry of the original Ω is poorly correlated with the new idealized $\widetilde{\Omega}$.

Following the rotation, C_Ω climbs for a period of time, but then decreases again, indicating that the vorticity field deviates from the ideal plate-like configuration rather than approaching it. This result implies that the original weak zones have a very long term effect on the plate evolution after a motion change. In particular, the new (post-rotation) strike-slip plate boundaries are suboptimal for idealized plate motion (relative to the orientation of the driving force or source-sink field) for extended periods. Using the source-sink rate scale S discussed in §2.5.1, the dimensional duration of the experiments is of order several 10Myrs. The grain-damage and pinning mechanism thus allows for suboptimal plate boundary evolution akin to the evolution of the San Andreas fault

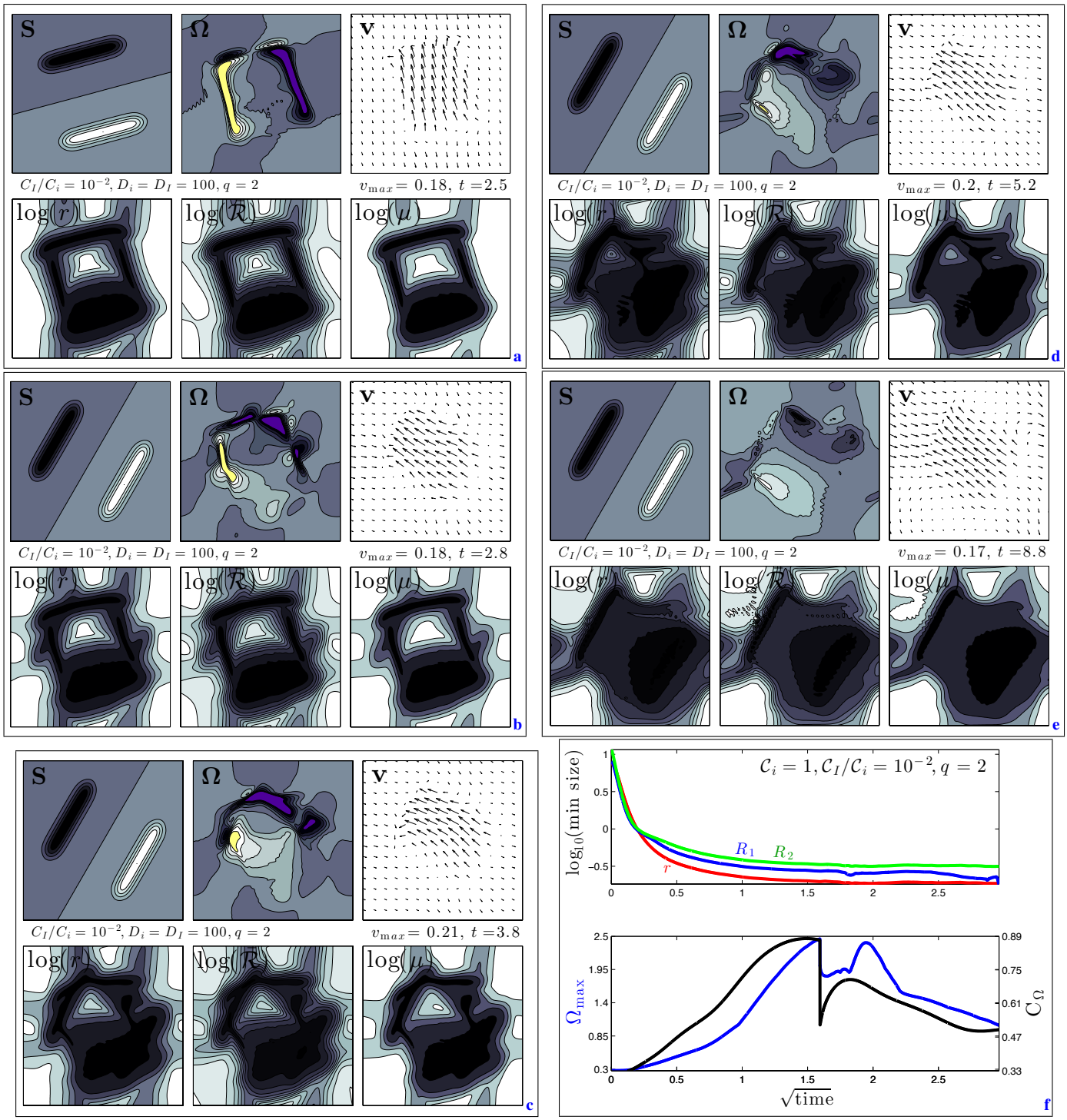

Figure 6: Experiment to show effect of weak-zone inheritance after change in plate motion. Frames a-e show the same fields as in Fig. 2a, at different times; frame a is just before the change in source-sink motion from its W15N direction; frames b-e are after the source-sink motion is re-oriented to W60N. Frame f shows the same time evolution of extremum quantities as in Fig. 2b; the sudden change in quantities, especially the abrupt drop in C_Ω, indicates the time at which the source-sink sink field is rotated. The experiment is for $q = 2$, and interface healing rate $C_\mathrm{I} = 10^{-2}$ (and $C_i = 1$). Extrema ([min,max]) in contour plots for Ω, r, $\bar{\mathcal{R}}$ and μ are (a) [-2.2,2.5], [0.2,3.8], [0.3,3.7] and [0.02,9.2], respectively; (b) [-1.7,1.8], [0.2,3.7], [0.3,3.5] and [0.02,9.0], respectively; (c) [-2.4,1.5], [0.2,3.2], [0.3,3.2] and [0.01,8.4], respectively; (d) [-1.5,1.1], [0.2,2.7], [0.3,2.9] and [0.01,7.6], respectively; and (e) [-1.0,0.7], [0.2,1.9], [0.3,2.5] and [0.01,6.0], respectively.

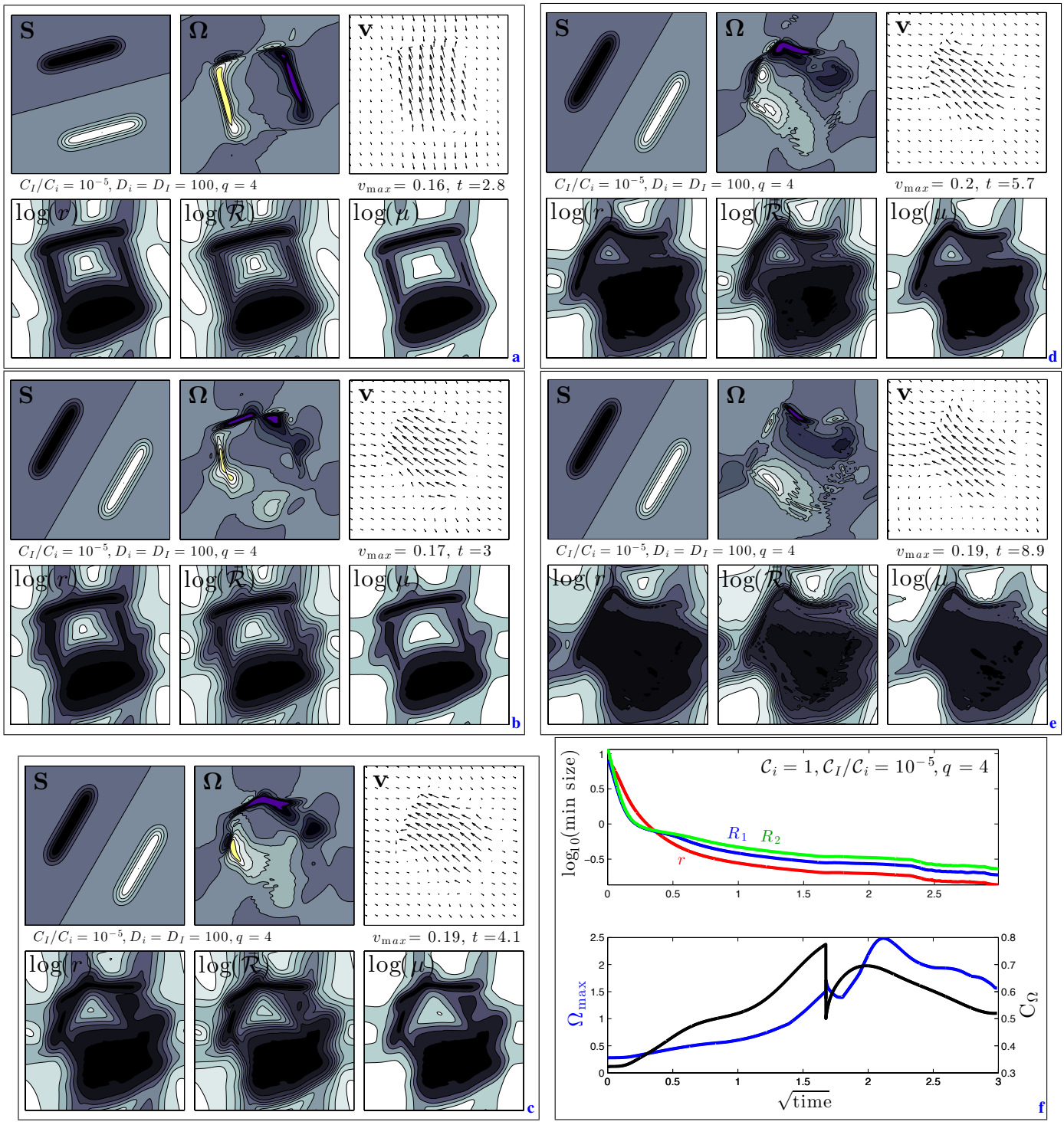

Figure 7: Same as Fig 6 but with $q = 4$ and $C_I = 10^{-5}$. Extrema ([min,max]) in contour plots for Ω, r, $\bar{\mathcal{R}}$ and μ are (a) [-1.3,1.5], [0.2,4.9], [0.3,3.7] and [0.02,9.3], respectively; (b) [-1.4,1.1], [0.2,4.8], [0.3,3.6] and [0.02,9.1], respectively; (c) [-2.3,1.4], [0.2,4.3], [0.3,3.3] and [0.01,8.6], respectively; (d) [-2.0,1.0], [0.2,3.7], [0.3,3.0] and [0.01,8.0], respectively; and (e) [-1.6,0.9], [0.1,2.8], [0.2,2.7] and [0.01,6.9], respectively.

(SAF) system over the last 20Myrs (that boundary, however, was a subduction zone prior to 20Ma).

3.3.3. Evolving plate asymmetry

Another important feature of the experiment is the evolving asymmetry in the plate motion as well as plate boundary structure. In particular, the "northernmost" end-point of the sink field (or subduction zone) forms an accute corner with the relic vorticity field (strike-slip margin) that connects to it, while the southernmost end-point of the sink forms an obtuse angle with the relic vortex (e.g., see Fig. 7c-e). The norther acute angle generates very high strain-rates and damage, and thus causes a sharp and high-amplitude vorticity peak which persists throughout the experiment. The southern obtuse angle has much less strain rate and does not undergo the same degree of damage. The end result is that the two vortex fields (the right-lateral margin to the north and the left-lateral one in the south) are asymmetric, with the northern one being more intense. This has two pronounced effects. First the northern acute corner generates a long-lived weak plate corner that is similar to the sharp Aleutian-Kurile arc corner (i.e., where the old sink is analogous to the pre-47Ma Aleutian trench, now transitioned into a zone of large strike-slip vorticity associated with highly oblique subduction; and the new sink is akin to the current Kurile and Western Pacific trench system), which has persisted for tens of millions of years despite the fact that it is an ocean-ocean boundary with no continental shelf to stabilize such a sharp structure (although the effect of subducting the Emperor chain at this corner remains an open question). Secondly, the strong northern vortex causes the plate motion to actually evolve slightly away from the source-sink orientation; i.e., immediately after the source-sink rotation, the flow velocities are largely orientated in a W60N direction (e.g., Fig. 7b), but as the plate boundaries evolve the flow direction is pulled gradually north toward the strong corner vortex, leading to oblique convergence or subduction (Fig. 7e).

Although the overall evolution of the experiments are qualitatively similar for the $q = 2$ and $q = 4$ cases, the asymmetries in the velocity and vorticity fields are more pronounced for the $q = 4$ experiments. In particular, the final northern acute vorticity maximum for the $q = 4$ case (Fig. 7e) is 60% larger than the peak amplitude of the source-sink field, the peak idealized vorticity field (see (29)) as well as the peak vorticity for the $q = 2$ case (Fig. 6e). Indeed, the exponent $q = 4$ is the most likely value based on comparison to polycrystalline coarsening experiments (Hiraga et al., 2010; Bercovici and Ricard, 2012) since it is associated with stagnant grain growth at large times; it is this very behavior that impedes healing, sustains relic weak zones and causes more severe asymmetries in our plate reorganization experiments.

In the end, the grain-damage and pinning model of plate generation allows the memory of an original plate configuration to persist after an abrupt motion change, and to affect the evolution and structure of the re-oriented plate for geologically extended periods.

4. Discussion and Conclusion

As discussed in Bercovici and Ricard (2012), the grain-damage and pinning mechanism solves several significant quandaries with regard to plate generation and deep lithospheric shear localization. First it permits grain-reducing damage to co-exist with grain-size dependent diffusion creep, thus enabling a shear-localizing and self-weakening mechanism in the deep lithosphere. Without Zener pinning, grain-reduction occurs while the material is undergoing dislocation creep, which is unaffected by grain-size, and grain-size dependent rheology only occurs in diffusion creep, in which the grains cannot shrink. (While some combination of stress- and grainsize-dependent rheology can occur close to the diffusion-dislocation creep boundary, such as due to mixing of grain-sizes or grain-boundary sliding, the resultant rheology is still fixed close this boundary, thus leading to weak or modest feedbacks and localization.) With Zener pinning in a two-phase or polycrystalline material such as peridotite, damage to the interface between phases increases the number of small blocking or pinning surfaces, which then reduce grain-size even while well into the diffusion creep regime.

In this paper we have tested this self-softening feedback mechanism for its efficacy in generating plate-like toroidal motion, which is one of the key metrics of plate generation. The simple test is a source-sink model used previously (Bercovici, 1993, 1995, 1998; Bercovici and Ricard, 2005) and we compare the results to two baseline cases, i.e., pure dislocation creep and a grain-damage mechanism without pinning. Both baseline cases produce very nearly identical weak localization and toroidal motion. In contrast the model with grain-damage and Zener pinning is capable of producing significant localization and large focussed toroidal motion, highly plate-like velocity and viscosity fields, in addition to grain-size reduction consistent with peridotitic mylonites (e.g., Warren and Hirth, 2006; Linckens et al., 2011); see §3.2.3. If such localization is dominant in the lower lithosphere below plate boundaries, then lattice preferred orientation (LPO) in olivine undergoing dislocation creep should be weakened and possibly detectable as a lack of seismic anisotropy. While there is some indication of this effect from field studies (e.g., Mehl and Hirth, 2008), the expression of such low-LPO features in regional seismic anisotropy is doubtful (Warren and Hirth, 2006, M. D. Long, *pers. comm.*), and resolution would require analysis with higher-frequency waves and removing signals of shallow fabric (e.g., laminae or cracks). Nevertheless, refined seismic studies of plate boundaries would provide an important test for these models.

Damage theories of plate generation are further able to treat plate boundary evolution, in particular the effect of dormant plate boundaries that can be reactivated, or relic boundaries after plate-motion changes. With the source-sink model we are able to experiment with the effect of rapid plate motion change similar to that associated with the Emperor-Hawaiian bend. In these experiments the relic strike-slip weak zones prior to the plate motion change have a long-lived influence on the new plate

motion, causing the plate boundaries to have suboptimal orientation, i.e., strike-slip margins non-orthogonal to the convergent/divergent boundaries, as evident in the San Andreas system. Moreover, the rotation causes an asymmetry in the flow field that induces oblique subduction and a weak acute corner similar to the Aleutian-Kurile junction that is an ocean-ocean boundary with no continental structure to stabilize such a sharp feature.

In the end, the grain-damage and Zener pinning model of plate-generation is, according to the tests performed herein, able to sustain deep lithospheric localization, excite substantial toroidal flow from convective-type motion, and permits dormant or relic weak zones and plate boundaries that profoundly influence plate tectonic evolution.

Acknowledgments. The authors thank Lars Hansen and an anonymous reviewer for their very helpful comments and suggestions. Support was provided by the National Science Foundation (NSF, grant EAR-1015229), the Agence Nationale de la Recherche (Labex LIO), the Yale Amity Geophysical Annex (YAGA) and Le Garon Foundation for Supine Geophysics (GFSG).

References

Abbott, P. L., 2011. Natural Disasters, 8th Edition. McGraw-Hill, Inc.

Austin, N., Evans, B., 2007. Paleowattmeters: A scaling relation for dynamically recrystallized grain size. Geology 35, 343–346.

Auth, C., Bercovici, D., Christensen, U., 2003. Two-dimensional convection with a self-lubricating, simple-damage rheology. Geophys. J. Int. 154, 783–800.

Bercovici, D., 1993. A simple model of plate generation from mantle flow. Geophys. J. Int. 114, 635–650.

Bercovici, D., 1995. A source-sink model of the generation of plate tectonics from non-newtonian mantle flow. J. Geophys. Res. 100, 2013–2030.

Bercovici, D., 1998. Generation of plate tectonics from lithosphere-mantle flow and void-volatile self-lubrication. Earth Planet. Sci. Lett. 154, 139–151.

Bercovici, D., 2003. The generation of plate tectonics from mantle convection. Earth Planet. Sci. Lett. 205, 107–121.

Bercovici, D., Ricard, Y., 2003. Energetics of a two-phase model of lithospheric damage, shear localization and plate-boundary formation. Geophys. J. Intl. 152, 581–596.

Bercovici, D., Ricard, Y., 2005. Tectonic plate generation and two-phase damage: void growth versus grainsize reduction. J. Geophys. Res. 110, B03401, doi:10.1029/2004JB003181.

Bercovici, D., Ricard, Y., 2012. Mechanisms for the generation of plate tectonics by two-phase grain-damage and pinning. Phys. Earth Planet. Int. 202-203, 27–55.

Bercovici, D., Ricard, Y., Richards, M., 2000. The relation between mantle dynamics and plate tectonics: A primer. In: Richards, M. A., Gordon, R., van der Hilst, R. (Eds.), History and Dynamics of Global Plate Motions, Geophys. Monogr. Ser. Vol. 121. Am. Geophys. Union, Washington, DC, pp. 5–46.

Bercovici, D., Ricard, Y., Schubert, G., 2001a. A two-phase model of compaction and damage, 1. general theory. J. Geophys. Res. 106 (B5), 8887–8906.

Bercovici, D., Ricard, Y., Schubert, G., 2001b. A two-phase model of compaction and damage, 3. applications to shear localization and plate boundary formation. J. Geophys. Res. 106 (B5), 8925–8940.

Braun, J., Chery, J., Poliakov, A., Mainprice, D., Vauchez, A., Tomassi, A., Daignieres, M., 1999. A simple parameterization of strain localization in the ductile regime due to grain size reduction: A case study for olivine. J. Geophys. Res. 104, 25167–25181.

Charbonneau, D., Berta, Z. K., Irwin, J., Burke, C. J., Nutzman, P., Buchhave, L. A., Lovis, C., Bonfils, X., Latham, D. W., Udry, S., Murray-Clay, R. A., Holman, M. J., Falco, E. E., Winn, J. N., Queloz, D., Pepe, F., Mayor, M., Delfosse, X., Forveille, T., 2009. A super-earth transiting a nearby low-mass star. Nature 462, 891–894.

Davies, G., Richards, M., 1992. Mantle convection. J. Geology 100, 151–206.

De Bresser, J., Peach, C., Reijs, J., Spiers, C., 1998. On dynamic recrystallization during solid state flow: effects of stress and temperature. Geophys. Res. Lett. 25, 3457–3460.

De Bresser, J., ter Heege, J., Spiers, C., 2001. Grain size reduction by dynamic recrystallization: can it result in major rheological weakening? Intl. J. Earth Sci. 90, 28–45.

Derby, B., Ashby, M., 1987. On dynamic recrystallization. Scripta Metallurgica 21, 879–884.

Doherty, R. D., Hughes, D. A., Humphreys, F. J., Jonas, J. J., Jensen, D. J., Kassner, M. E., King, W. E., McNelley, T. R., McQueen, H. J., Rollett, A. D., 1997. Current issues in recrystallization: a review. Materials Science and Engineering A 238 (2), 219–274.

Etheridge, M., Wilkie, J., 1979. Grainsize reduction, grain boundary sliding and the flow strength of mylonites. Tectonophysics 58 (1-2), 159–178, microstructural processes during deformation and metamorphism.

Foley, B., Becker, T., 2009. Generation of plate-like behavior and mantle heterogeneity from a spherical, visco-plastic convection model. Geochem., Geophys., Geosys. 10 (8), Q08001, doi:10.1029/2009GC002378.

Foley, B. J., Bercovici, D., Landuyt, W., 2012. The conditions for plate tectonics on super-earths: Inferences from convection models with damage. Earth and Planetary Science Letters 331-332, 281–290.

Furusho, M., Kanagawa, K., 1999. Reaction induced strain localization in a lherzolite mylonite from the hidaka metamorphic belt of central hokkaido, japan. Tectonophysics 313, 411–432.

Gurnis, M., Zhong, S., Toth, J., 2000. On the competing roles of fault reactivation and brittle failure in generating plate tectonics from mantle convection. In: Richards, M. A., Gordon, R., van der Hilst, R. (Eds.), History and Dynamics of Global Plate Motions, Geophys. Monogr. Ser. Vol. 121. Am. Geophys. Union, Washington, DC, pp. 73–94.

Hager, B., O'Connell, R., 1979. Kinematic models of large-scale flow in the earth's mantle. J. Geophys. Res. 84, 1031–1048.

Hager, B., O'Connell, R., 1981. A simple global model of plate dynamics and mantle convection. J. Geophys. Res. 86, 4843–4867.

Hall, C. E., Gurnis, M., Sdrolias, M., Lavier, L. L., Mueller, R. D., 2003. Catastrophic initiation of subduction following forced convergence across fracture zones. Earth Planet. Sci. Lett 212, 15–30.

Hansen, L. N., Zimmerman, M. E., Kohlstedt, D. L., 2012. The influence of microstructure on deformation of olivine in the grain-boundary sliding regime. J. Geophys. Res. 117, B09201.

Herwegh, M., Linckens, J., Ebert, A., Berger, A., Brodhag, S., 2011. The role of second phases for controlling microstructural evolution in polymineralic rocks: A review. Journal of Structural Geology 33 (12), 1728 – 1750.

Hillert, M., 1988. Inhibition of grain growth by second-phase particles. Acta Metallurgica 36 (12), 3177 – 3181.

Hiraga, T., Tachibana, C., Ohashi, N., Sano, S., 2010. Grain growth systematics for forsterite ± enstatite aggregates: Effect of lithology on grain size in the upper mantle. Earth Planet. Sci. Lett. 291, 10–20.

Hirth, G., Kohlstedt, D., 2003. Rheology of the upper mantle and the mantle wedge: a view from the experimentalists. In: Eiler, J. (Ed.), Subduction Factor Mongraph. Vol. 138. Am. Geophys. Union, Washington, DC, pp. 83–105.

Jin, D., Karato, S., Obata, M., 1998. Mechanisms of shear localization in the continental lithosphere: Inference from the deformation microstructures of peridotites from the ivrea zone, northwestern italy. J. Struct. Geol. 20, 195–209.

Kameyama, M., Yuen, D., Fujimoto, H., 1997. The interaction of viscous heating with grain-size dependent rheology in the formation of localized slip zones. Geophys. Res. Lett. 24, 2523–2526.

Karato, S., 1989. Grain growth kinetics in olivine aggregates. Tectonophysics 168, 255–273.

Karato, S., 2008. Deformation of Earth Materials: An Introduction to the Rheology of Solid Earth. Cambridge Univ. Press.

Karato, S., Toriumi, M., Fujii, T., 1980. Dynamic recrystallization of olivine single crystals during high temperature creep. Geophys. Res. Lett. 7, 649–652.

Karato, S., Wu, P., 1993. Rheology of the upper mantle: A synthesis. Science 260, 771–778.

Kaula, W., 1980. Material properties for mantle convection consistent with ob-

served surface fields. J. Geophys. Res. 85, 7031–7044.
Korenaga, J., 2010. On the likelihood of plate tectonics on super-earths: Does size matter? Astrophys. J. Lett. 725 (1), L43–L46.
Landuyt, W., Bercovici, D., 2009a. Formation and structure of lithospheric shear zones with damage. Phys. Earth Planet. Int.Doi:10.1016/j.pepi.2009.03.005.
Landuyt, W., Bercovici, D., 2009b. Variations in planetary convection via the effect of climate on damage. Earth Planet. Sci. Lett. 277, 29–37.
Landuyt, W., Bercovici, D., Ricard, Y., 2008. Plate generation and two-phase damage theory in a model of mantle convection. Geophys. J. Int. 174, 1065–1080.
Lebrun, J.-F., Lamarche, G., Collot, J.-Y., 2003. Subduction initiation at a strike-slip plate boundary: The cenozoic pacific-australian plate boundary, south of new zealand. J. Geophys. Res. 108, 2453, doi:10.1029/2002JB002041.
Lee, K., Jiang, Z., Karato, S., 2002. A scanning electron microscope study of effects of dynamic recrystallization on the lattice preferred orientation in olivine. Tectonophysics 351, 331–341.
Linckens, J., Herwegh, M., Müntener, O., Mercolli, I., 2011. Evolution of a polymineralic mantle shear zone and the role of second phases in the localization of deformation. J. Geophys. Res. 116, B06210, 21 pp.
McKenzie, D., 1981. The variation of temperature with time and hydrocarbon maturation in sedimentary basins formed by extension. Earth and Planetary Science Letters 55 (1), 87 – 98.
Mehl, L., Hirth, G., 2008. Plagioclase preferred orientation in layered mylonites: Evaluation of flow laws for the lower crust. J. Geophys, Res. 113 (B05202), doi:10.1029/2007JB005075.
Montési, L., Hirth, G., 2003. Grain size evolution and the rheology of ductile shear zones: From laboratory experiments to postseismic creep. Earth Planet. Sci. Lett. 211, 97–110.
Olgaard, D., 1990. The role of second phase in localizing deformation. In: Knipe, R., Rutter, E. (Eds.), Deformation Mechanisms, Rheology and Tectonics. 54. Geological Society Special Publication, pp. 175–181.
O'Neill, C., Lenardic, A., 2007. Geological consequences of super-sized earths. Geophys. Res. Lett. 34, 19204—19208.
Ricard, Y., Bercovici, D., 2003. Two-phase damage theory and crustal rock failure: the theoretical 'void' limit, and the prediction of experimental data. Geophys. J. Int. 155, 1057–1064.
Ricard, Y., Bercovici, D., 2009. A continuum theory of grain size evolution and damage. J. Geophys. Res. 114, B01204, doi:10.1029/2007JB005491.
Ricard, Y., Vigny, C., 1989. Mantle dynamics with induced plate tectonics. J. Geophys. Res. 94, 17543–17559.
Richards, M., Yang, W.-S., Baumgardner, J., Bunge, H.-P., 2001. Role of a low-viscosity zone in stabilizing plate tectonics: Implications for comparative terrestrial planetology. Geochem. Geophys. Geosystems (G^3) 2, 2000GC000115.
Rozel, A., Ricard, Y., Bercovici, D., 2011. A thermodynamically self-consistent damage equation for grain size evolution during dynamic recrystallization. Geophys. J. Int. 184 (2), 719–728.
Sharp, W. D., Clague, D. A., 2006. 50-ma initiation of hawaiian-emperor bend records major change in pacific plate motion. Science 313 (5791), 1281–1284.
Shimizu, I., 1998. Stress and temperature dependence of recrystallized grain size: a subgrain misorientation model. Geophys. Res. Lett. 25, 4237–4240.
Smith, C. S., 1948. Grains, phases, and interfaces: An interpretation of microstructure. Trans. A.I.M.E. 175, 15–51.
Solomatov, V., El-Khozondar, R., Tikare, V., 2002. Grain size in the lower mantle: constraints from numerical modeling of grain growth in two-phase systems. Phys. Earth Planet. Int. 129, 265–282.
Southam, G., Westall, F., 2007. Geology, life and habitability. In: Tilman Spohn (Gerald Schubert, Ed.-in-Chief) (Ed.), Treatise on Geophysics. Vol. 10, *Planets & Moons*. Elsevier, Amsterdam, pp. 421 – 437.
Stein, C., Schmalzl, J., Hansen, U., 2004. The effect of rheological parameters on plate behaviour in a self-consistent model of mantle convection. Phys. Earth Planet. Int. 142, 225–255.
Tackley, P., 1998. Self-consistent generation of tectonic plates in three-dimensional mantle convection. Earth Planet. Sci. Lett. 157, 9–22.
Tackley, P., 2000a. The quest for self-consistent generation of plate tectonics in mantle convection models. In: Richards, M. A., Gordon, R., van der Hilst, R. (Eds.), History and Dynamics of Global Plate Motions, Geophys. Monogr. Ser. Vol. 121. Am. Geophys. Union, Washington, DC, pp. 47–72.
Tackley, P., 2000b. Self-consistent generation of tectonic plates in time-dependent, three-dimensional mantle convection simulations, 1. pseudoplastic yielding. Geochem. Geophys. Geosystems (G^3) 1, 2000GC000036.
Tackley, P., 2000c. Self-consistent generation of tectonic plates in time-dependent, three-dimensional mantle convection simulations, 2. strain weakening and asthenosphere. Geochem. Geophys. Geosystems (G^3) 1, 2000GC000043.
Toth, G., Gurnis, M., 1998. Dynamics of subduction initiation at preexisting fault zones. J. Geophys. Res. 103, 18053–18067.
Trompert, R., Hansen, U., 1998. Mantle convection simulations with rheologies that generate plate-like behavior. Nature 395, 686–689.
Urai, J., Means, W., Lister, G., 1986. Dynamic recrystallization in minerals. In: Hobbs, B., Heard, H. (Eds.), Mineral and Rock Deformation: Laboratory Studies. American Geophysical Union, Washington DC, pp. 166–199.
Valencia, D., O'Connell, R., Sasselov, D., 2007. Inevitability of plate tectonics on super-earths. Astrophys. J. 670, L45–L48.
Valencia, D., O'Connell, R. J., 2009. Convection scaling and subduction on earth and super-earths. Earth and Planetary Science Letters 286 (3-4), 492 – 502.
van Heck, H., Tackley, P., 2008. Planforms of self-consistently generated plates in 3d spherical geometry. Geophys. Res. Lett. 35, L19312, doi:10.1029/2008GL035190.
van Heck, H., Tackley, P., 2011. Plate tectonics on super-earths: Equally or more likely than on earth. Earth and Planetary Science Letters 310 (3–4), 252–261.
Vigny, C., Ricard, Y., Froidevaux, C., 1991. The driving mechanism of plate tectonics. Tectonophysics 187, 345–360.
Walker, J., Hayes, P., Kasting, J., 1981. A negative feedback mechanism for the long-term stabilization of Earth's surface temperature. J. Geophys. Res. 86, 9776–9782.
Warren, J. M., Hirth, G., 2006. Grain size sensitive deformation mechanisms in naturally deformed peridotites. Earth Planet. Sci. Lett. 248 (1-2), 438–450.
Weinstein, S., Olson, P., 1992. Thermal convection with non-newtonian plates. Geophys. J. Int. 111, 515–530.
White, S., Burrows, S., Carreras, J., Shaw, N., Humphreys, F., 1980. On mylonites in ductile shear zones. J. Struct. Geol. 2, 175–187.